Research
A SCIENCE PARTNER JOURNAL

REVIEW ARTICLE

A Review of Intense Electromagnetic Fields in Heavy-Ion Collisions: Theoretical Predictions and Experimental Results

Diyu Shen[1,2], Jinhui Chen[1,3], Xu-Guang Huang[1,3,4], Yu-Gang Ma[1,3*], Aihong Tang[5], and Gang Wang[6]

[1]Key Laboratory of Nuclear Physics and Ion-Beam Application (MOE), Institute of Modern Physics, Fudan University, Shanghai 200433, China. [2]Heavy Ion Science and Technology Key Laboratory, Institute of Modern Physics, Chinese Academy of Sciences, Lanzhou 730000, China. [3]Shanghai Research Center for Theoretical Nuclear Physics, NSFC and Fudan University, Shanghai 200438, China. [4]Physics Department and Center for Particle Physics and Field Theory, Fudan University, Shanghai 200438, China. [5]Brookhaven National Laboratory, Upton, NY 11973, USA. [6]Department of Physics and Astronomy, University of California, Los Angeles, CA 90095, USA.

*Address correspondence to: mayugang@fudan.edu.cn

Citation: Shen D, Chen J, Huang XG, Ma YG, Tang A, Wang G. A Review of Intense Electromagnetic Fields in Heavy-Ion Collisions: Theoretical Predictions and Experimental Results. *Research* 2025;8:Article 0726. https://doi.org/10.34133/research.0726

Submitted 20 March 2025
Revised 10 May 2025
Accepted 11 May 2025
Published 24 June 2025

In heavy-ion collisions at relativistic energies, the incident nuclei travel at nearly the speed of light. These collisions deposit kinetic energy into the overlap region and create a high-temperature environment where hadrons "melt" into deconfined quarks and gluons. The spectator nucleons, which do not undergo scatterings, generate an ultraintense electromagnetic field—on the order of 10^{18} G at the Relativistic Heavy Ion Collider and 10^{19} G at the Large Hadron Collider. These powerful electromagnetic fields have a substantial impact on the produced particles, not only complicating the study of particle interactions but also inducing novel physical phenomena. To explore the nature of these fields and their interactions with deconfined quarks, we provide a detailed overview, encompassing theoretical estimations of their generation and evolution, as well as experimental efforts to detect them. We also provide physical interpretations of the discovered results and discuss potential directions for future investigations.

Introduction

Heavy-ion collision experiments investigate the properties of nuclear matter under extreme temperatures and energy densities by smashing atomic nuclei at ultrahigh center-of-mass energies ($\sqrt{s_{NN}}$). A primary goal is to create and study the quark–gluon plasma (QGP) [1], a state of matter in which quarks and gluons are no longer confined within color-neutral hadrons, resembling conditions in the early universe following the big bang [2]. The 2 major facilities conducting such experiments are the Relativistic Heavy Ion Collider (RHIC) at Brookhaven National Laboratory and the Large Hadron Collider (LHC) at the European Organization for Nuclear Research. At these laboratories, heavy ions, such as copper (Cu), gold (Au), and lead (Pb), are accelerated to relativistic speeds (greater than 0.99c, where c denotes the speed of light in vacuum). Measurements from such experiments provide crucial insights into quantum chromodynamics (QCD), including the phase transition between ordinary nuclear matter and QGP, chiral symmetry restoration, and the violation of P (parity) and CP (charge-parity) symmetries in strong interactions [3–6].

In heavy-ion collisions, the relativistic charged protons within nuclei generate intense magnetic fields, reaching strengths of approximately 10^{18} G at the RHIC and 10^{19} G at the LHC [7–9]. Such immense field strengths make electromagnetic interactions nonnegligible compared with the energy scale of the strong interaction in the QGP [10]. Initial interest in these magnetic fields arose from studies of the chiral magnetic effect (CME) in heavy-ion collisions [8,11]. The CME describes the induction of an electric current along the magnetic field direction if the quarks in the QGP possess a net chirality [8,11–13]. Chirality refers to the intrinsic handedness of quarks: right-handed (left-handed) quarks have spin projections aligned (antialigned) with their momentum direction, whereas for antiparticles, this relationship is reversed. In addition to the deconfinement phase transition, light quarks are expected to undergo a chiral phase transition at high temperatures, restoring chiral symmetry, becoming almost massless, and acquiring a definite chirality [14]. Meanwhile, the gluon fields in the QCD vacuum can undergo topological transitions that violate P and CP symmetries, transferring a net chirality to quarks in the QGP [8,11,12]. Thus, heavy-ion collisions can satisfy both necessary conditions for the CME: a strong magnetic field and a net chirality in the QGP. In addition to the CME, strong magnetic fields can markedly influence QCD phase transitions. They may act as catalysts for chiral symmetry breaking at low temperature [15], suppress the temperatures at which

chiral phase transitions occur [16,17], and alter the critical endpoint in the QCD phase diagram, where the phase transition shifts from first order to a crossover [18–20]. Strong magnetic fields are also prevalent in astrophysical systems, such as neutron stars, where surface magnetic fields can reach 10^{12} to 10^{13} G. These extreme conditions have spurred research into neutron star structure and the equation of state of neutron matter under intense magnetic fields [21–23]. Heavy-ion collision experiments offer a unique opportunity to investigate these phenomena in a controlled laboratory setting. Because of these interests, this article mainly focuses on the magnetic field, although the electric field could also be nonnegligible on an event-by-event basis.

Although classical electrodynamics can reliably estimate the maximum strength of the magnetic field in heavy-ion collisions [7–9,24,25], its temporal evolution remains an open theoretical question. The complexities arise from the interplay between the magnetic field and the charge-conducting medium [10,26–31], which is governed by Maxwell's equations and highly sensitive to the temperature-dependent electric conductivity of the medium [32–34]. The preequilibrium properties of the medium also shape the magnetic field's strength, as the system transitions into hydrodynamic evolution [10]. Additionally, deviations from Ohm's law in the medium may affect the field's evolution [29], while recent studies suggest that the QGP fluid vorticity can extend its lifetime [31,35]. Due to these complexities, estimates of the magnetic field strength in the medium can vary by several orders of magnitude across different models [10,28,29,31,36–38].

The large theoretical uncertainties highlight the need for experimental investigations of the magnetic field in heavy-ion collisions. Various phenomena induced by a strong magnetic field can serve as experimental magnetometers, including the CME [8,11,12,14], charge-dependent collective motion [39–46], the polarization difference between Λ and $\overline{\Lambda}$ [47], transverse momentum (p_T) spectra of dilepton pairs [48,49], directed flow of direct photons [50–52], and baryon electric charge correlations [53,54]. In this article, we review and discuss recent experimental results related to these effects.

We organize this paper as follows: In The Electromagnetic Field Production, we discuss theoretical predictions of the magnetic field, including its strength and temporal evolution across different models. Experimental Results of the Electromagnetic Field Effects reviews and analyzes experimental findings from various observables related to magnetic field detection. In Challenges and Opportunities, we outline key challenges and propose directions for future research. Finally, we summarize our conclusions in Summary.

The Electromagnetic Field Production

Nuclear-spectator-induced electromagnetic field

In heavy-ion collision experiments at relativistic energies, positively charged nuclei are accelerated to velocities approaching the speed of light. When these nuclei collide, the overlapping region can experience substantial energy deposition, potentially generating a deconfined QGP. However, in most collisions, the nuclei do not fully overlap. The transverse distance between the centers of the 2 incident nuclei is defined as the impact parameter b, as illustrated in Fig. 1. Collisions with $b = 0$ are conceptually referred to as the most central collisions, while those with b greater than the sum of the radii of the 2 nuclei are classified as ultraperipheral collisions (UPCs). In collisions with a finite b, spectator nucleons remain outside the overlapping region and do not directly participate in the interaction. The spectator protons, carrying positive charges and moving rapidly along the beam direction, generate an intense magnetic field in their vicinity.

The strength of the produced magnetic field can be calculated using the Liénard–Wiechert potentials, which are solutions to Maxwell's equations that describe the electromagnetic field produced by a moving point charge. Based on these potentials, the magnetic and electric fields are given by the following expressions:

$$e\mathbf{B}(t,\mathbf{r}) = \frac{e^2}{4\pi}\sum_n Z_n \frac{\mathbf{v}_n \times \mathbf{R}_n}{\left(R_n - \mathbf{R}_n\cdot\mathbf{v}_n\right)^3}\left(1-\left|\mathbf{v}_n\right|^2\right), \quad (1)$$

$$e\mathbf{E}(t,r) = \frac{e^2}{4\pi}\sum_n Z_n \frac{\mathbf{R}_n - R_n\mathbf{v}_n}{\left(R_n - \mathbf{R}_n\cdot\mathbf{v}_n\right)^3}\left(1-\left|\mathbf{v}_n\right|^2\right), \quad (2)$$

where Z_n is the electric charge of the nth particle and $\mathbf{R}_n = \mathbf{r} - \mathbf{r}_n$ is the distance vector between the field point $\mathbf{r}$ and the position $\mathbf{r}_n$ of the nth particle with velocity $\mathbf{v}_n$ at the retarded time $t_n = t - \left|\mathbf{r} - \mathbf{r}_n\right|$. t represents the moment at which the electromagnetic field is measured. These equations are fundamental in electrodynamics and are widely used to calculate the electric and magnetic fields generated by a charged particle moving with an arbitrary velocity. Although the Liénard–Wiechert potential is a classical formulation, it effectively describes the generation of electromagnetic fields in heavy-ion collisions, as quantum corrections to the Liénard–Wiechert potential play only a minor role in this context [55]. The primary uncertainty in calculating the produced electromagnetic field arises from the uncertain spatial distribution of spectator protons. An empirical model commonly used in nuclear physics, the Woods–Saxon distribution, describes the radial distribution of nuclear matter within an atomic nucleus, particularly for the nuclear potential or the spatial distribution of nucleons inside a nucleus. It is given by the following form [56–61]:

$$\rho(r,\theta,\phi) = \frac{\rho_0}{1+e^{\left[\frac{r-R(\theta)}{a}\right]}}, \quad (3)$$

$$R(\theta) = R_0\left[1+\beta_2 Y_2^0(\theta)+\beta_4 Y_4^0(\theta)+\ldots.\right], \quad (4)$$

where R_0 is the spherical radius, β_2 and β_4 are the deformation parameters (with β_2 typically representing the quadrupole deformation), and $Y_2^0(\theta)$ and $Y_4^0(\theta)$ are the spherical harmonics. The deformation parameters should be determined from experiments. For nearly spherical nuclei, such as gold (Au), a symmetric nucleon distribution is often used to estimate the strength of the electromagnetic field in Au + Au collisions at $\sqrt{s_{NN}} = 200$ GeV per nucleon pair, as shown in Fig. 2. The peak strength of the magnetic field in heavy-ion collisions at the RHIC could reach ~10^{18} G (1 G $\approx 1.95\times10^{-20}$ GeV^2), which is 10,000 times greater than the magnetic field of magnetars [62]. However, such a magnetic field decays quickly as the spectator protons move away. Figure 2 shows the time evolution of the magnetic field in a vacuum, where it becomes negligible compared with the peak value in ~10^{-24} s (1 fm/$c \approx 3.3\times10^{-24}$ s)

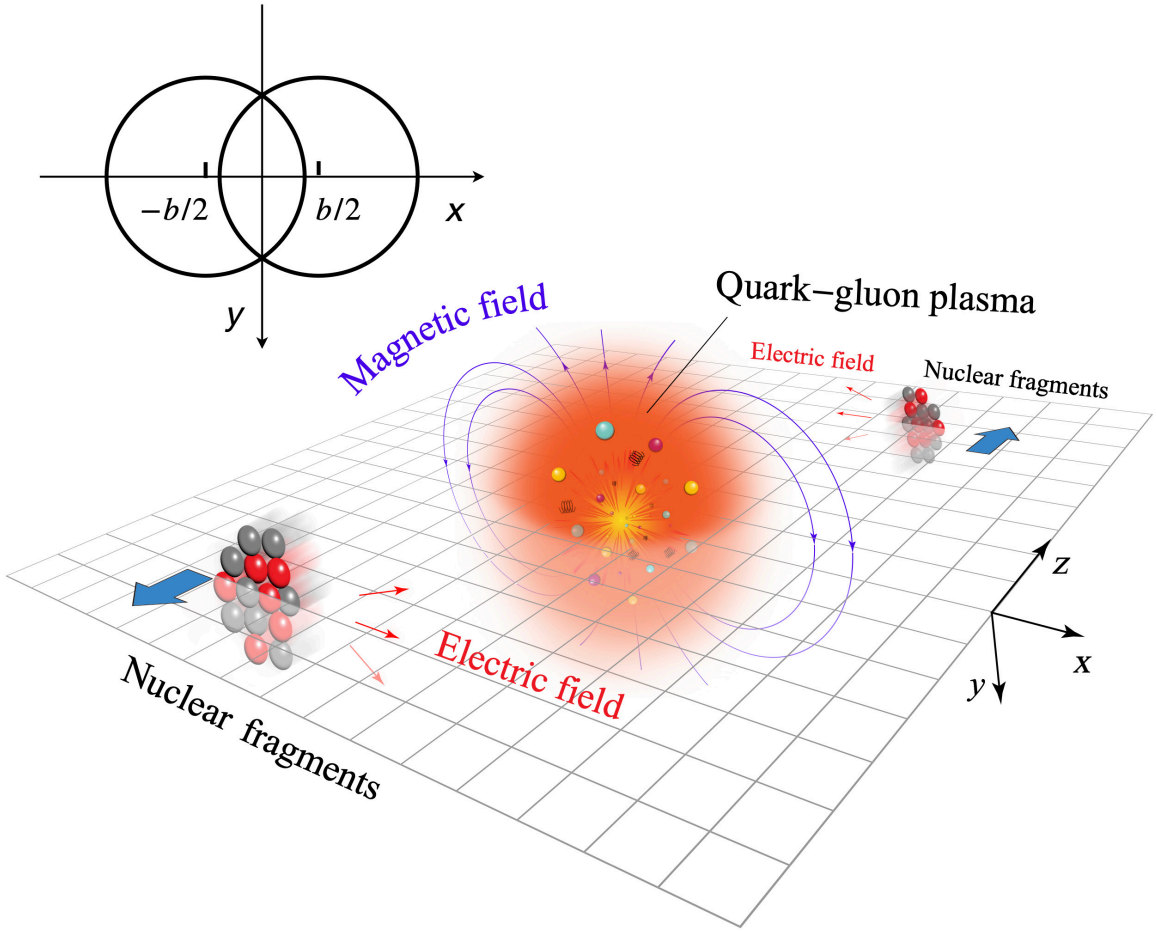

Fig. 1. Sketch of a heavy-ion collision in the lab frame (the figure is from Ref. [113]). The impact parameter and the beam direction are along the *x* and *z* axes, respectively. Spectator nuclear fragments generate strong magnetic fields along −*y*.

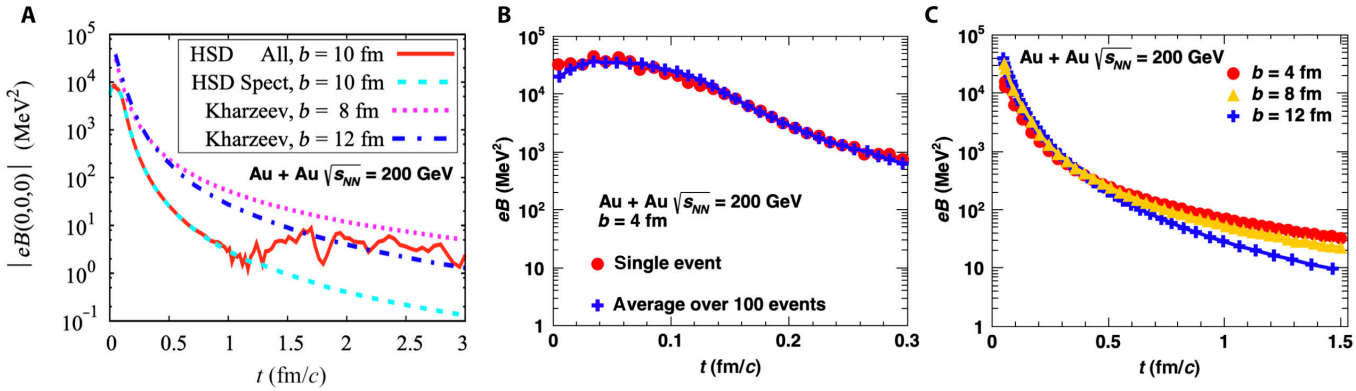

Fig. 2. Magnetic field produced mainly by spectator protons in semicentral Au + Au collisions at $\sqrt{s_{NN}}$ = 200 GeV, without medium responses, in (A) the Ultrarelativistic Quantum Molecular Dynamics (UrQMD) model [7], (B) the Hadron String Dynamics (HSD) model [37], and (C) semi-analytically, assuming infinitely thin nuclei [8]. (The figures are from Refs. [7,8,37].)

after the collision. Nevertheless, the presence of the QGP could prolong the lifetime of the magnetic field due to the Faraday induction effect, which is discussed in the next section.

The Liénard–Wiechert potentials show that the magnetic field generated by a moving charge depends on both the velocity and the number of source charges. This implies that the peak magnetic field strength is larger at higher collision energies and for larger impact parameters b as long as $b \lesssim 2R_0$. Such a relationship was confirmed by Skokov et al. [7], Deng and Huang [9], and Siddique et al. [63], as shown in Fig. 3. On the other hand, the initial structure of the colliding nuclei [64,65] is also important for the distribution of electromagnetic fields. For example, Cheng et al. [66] observed that the electric and magnetic fields display different behavioral patterns for asymmetric

combinations of the projectile and target nuclei as well as for different initial configurations of the nucleus.

Event-by-event magnetic field fluctuations

The spectator-induced magnetic field is, on average, aligned along the $-y$ axis over multiple events, as illustrated in Fig. 1, due to the mirror symmetry of the collision geometry. However, on an event-by-event basis, it fluctuates dramatically [9,24,67–69]. The strength and direction of the magnetic field depend on the spatial distribution and velocity of spectator protons, as indicated in Eq. (1). Although the velocity of protons is determined by the collision energy and beam direction—both known parameters—the spatial distribution of nucleons fluctuates event by event due to their quantum nature, leading to fluctuations in the magnetic field. Notably, it has been found that the magnetic field component along the impact parameter direction, B_x, can be comparable to B_y, as demonstrated in Fig. 4 [9,67]. Additionally, the electric field components, E_x and E_y, can be quite strong and are approximately equal in magnitude. More quantitatively, results from Deng and Huang [9] in Fig. 4A are 3 times smaller than those from Bzdak and Skokov [67] in Fig. 4B for central collisions. This discrepancy arises from differences in the nuclear thickness assumptions used in the calculations—Deng and Huang [9] accounted for a finite nuclear thickness, whereas Bzdak and Skokov [67] assumed infinitely thin nuclei, incorporating Lorentz contraction at $\sqrt{s_{NN}} = 200$ GeV.

The event-by-event magnetic field plays a crucial role in electromagnetic effects within the QGP, as it remains nonzero even in the most central collisions due to fluctuations in the spatial positions of protons. For instance, the CME describes charge separation on an event-by-event basis and depends only on the magnetic field of the specific event. Experimentally, CME signals are analyzed along directions reconstructed from final-state particles, conventionally referred to as event planes. A nonzero magnetic field in the most central collisions could influence our interpretation of CME measurements as a function of centrality.

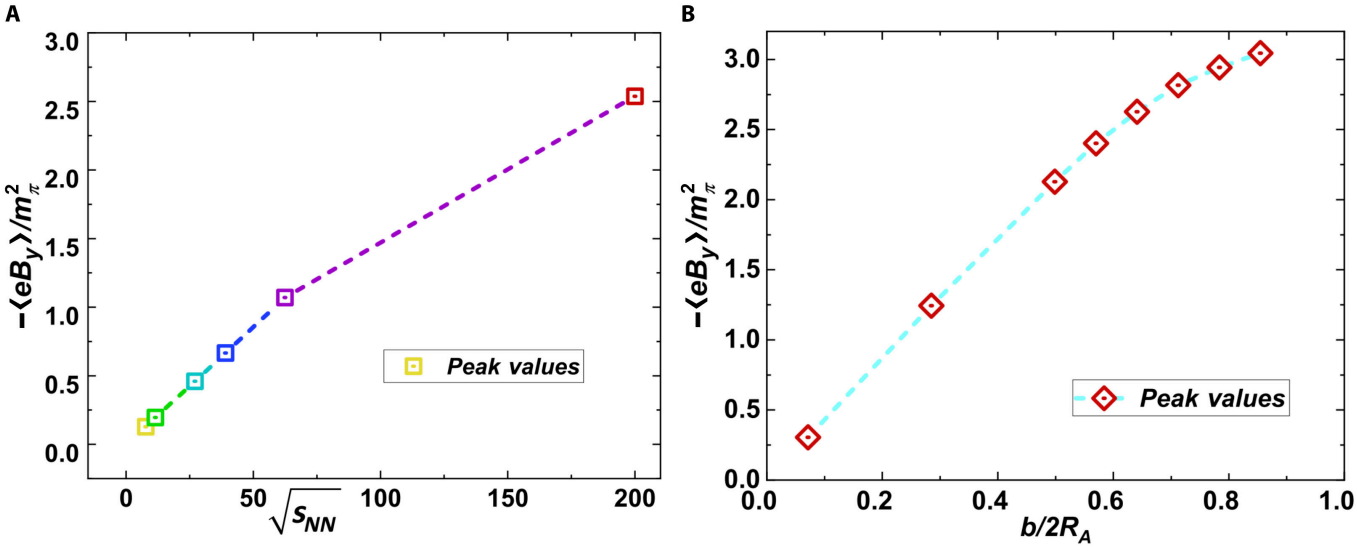

Fig. 3. The peak value of the magnetic field strength as a function of (A) collision energy and (B) impact parameter (the figure is from Ref. [63]).

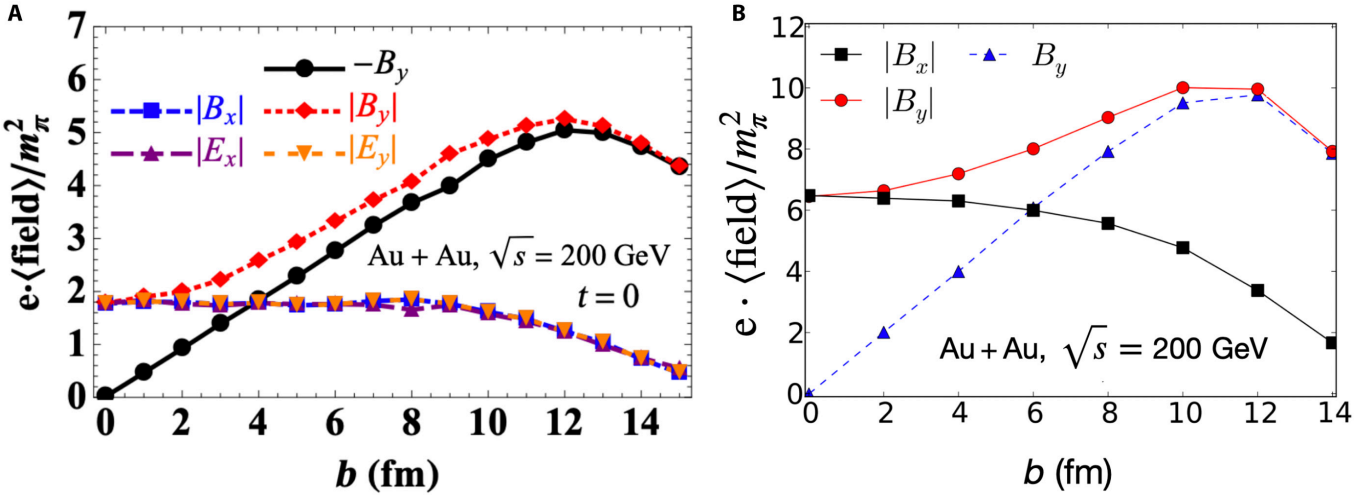

Fig. 4. Electromagnetic fields in Au + Au collisions at $\sqrt{s_{NN}} = 200$ GeV as functions of impact parameter b. The magnetic and electric field fluctuations are indicated by the magnitude averages along different directions. (A) Calculations using initial conditions from the Heavy Ion Jet INteraction Generator (HIJING) model (the figure is from [9]). (B) The initial nucleon distribution is from the Woods–Saxon distribution with standard parameters, assuming that both nuclei are infinitely thin (the figure is from Ref. [67]).

Zhao et al. [24] and Bloczynski et al. [68] investigated the correlations between the direction of the magnetic field and the event planes across different impact parameters. They found that the correlations between the magnetic field and the second-harmonic participant plane are largely suppressed in both very central and very peripheral collisions, while they peak in mid-central collisions, as illustrated in Fig. 5.

Time evolution of the magnetic field

While the electromagnetic field can be well estimated using the Liénard–Wiechert potentials, its time evolution remains an open question due to the complex interplay with the QGP. A time-varying magnetic field induces an electric field through Faraday induction, which, in turn, generates an electric current that counteracts the decay of the external magnetic field in an electrically conductive medium—a phenomenon known as Lenz's law. Figure 6A illustrates the evolution of the magnetic field in a static medium with different constant electrical conductivities [27], demonstrating that medium response substantially prolongs the field's lifetime. However, theoretical estimates of the QGP's electrical conductivity have large uncertainties, as it depends on the medium's temperature. The conductivity-to-temperature ratio, σ_{el}/T, extracted from lattice QCD [32,34,70,71], transport approaches [72,73], and effective models [74,75], spans 2 orders of magnitude, ranging from 0.001 to 0.4 for temperature from 0.1 to 0.6 GeV, as shown in Fig. 6B. In particular, substantial discrepancies exist between lattice QCD results and transport model predictions. These differences primarily arise because electrical conductivity reflects a nonequilibrium property of the QGP and is highly sensitive to how microscopic interactions are modeled in transport frameworks. For comparison, the QGP's conductivity estimated from parton–hadron–string dynamics is approximately 500 times larger than that of copper and silver at room temperature [72].

Moreover, the relaxation time of the medium response is also critical to the time evolution of the magnetic field. Li et al. [28] numerically solved Maxwell's equations in the QGP with a time-varying electric conductivity using the finite-difference-time-domain method. They found that the early-stage magnetic field is greatly suppressed when the conductivity becomes nonzero after the collision, compared to that of the case of constant conductivity. This suppression arises because the medium takes time to develop its effect on delaying the decay of the magnetic field. However, at later times, the magnetic fields in both cases converge and remain larger than that in the vacuum scenario, as illustrated in Fig. 7A.

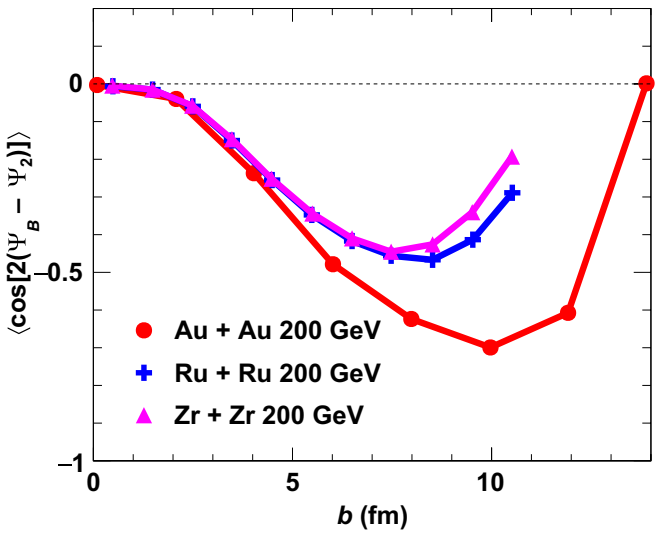

Fig. 5. Correlations between magnetic field and second-harmonic participant plane in Au + Au, Ru + Ru, and Zr + Zr collisions at $\sqrt{s_{NN}}$ = 200 GeV (the figure is from Refs. [24,68]). A more negative $\langle cosn(\Psi_B - \Psi_2)\rangle$ indicates a stronger correlation between the magnetic field and the participant plane Ψ_2.

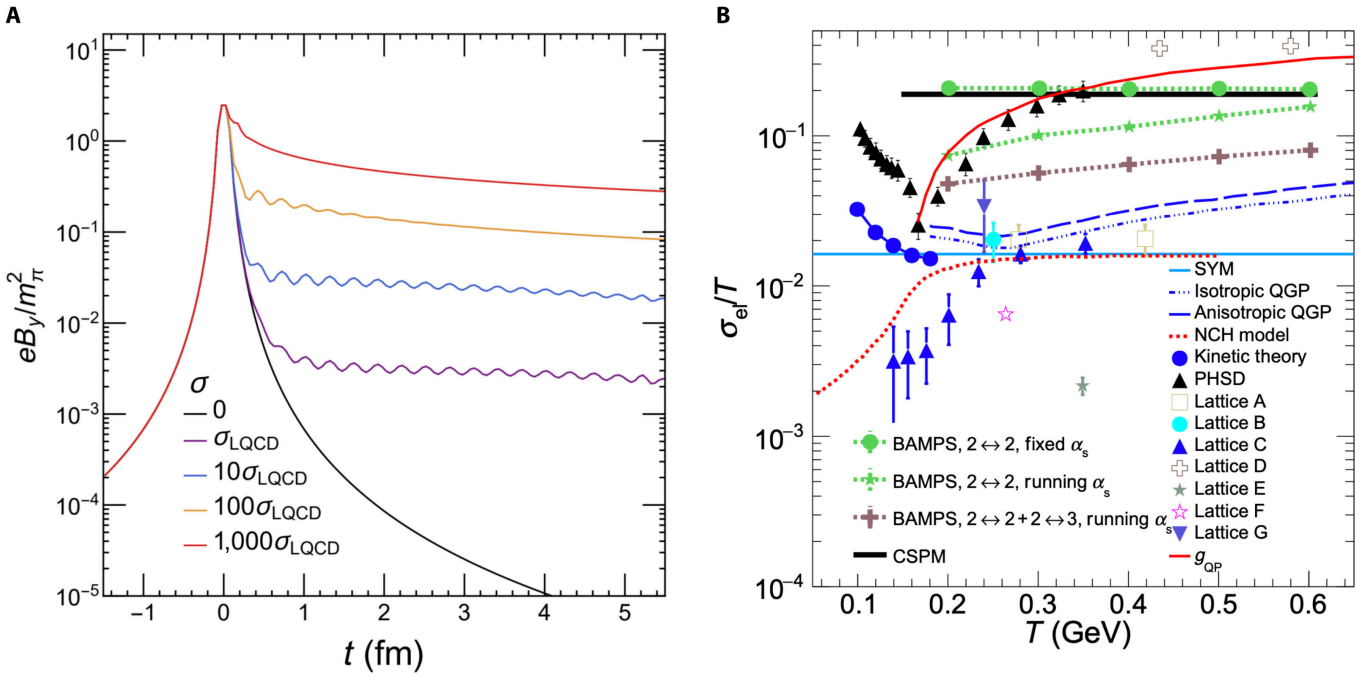

Fig. 6. (A) The magnetic field evolution with different electrical conductivities in Au + Au collisions at $\sqrt{s_{NN}}$ = 200 GeV with impact parameter b = 6 fm (the figure is from Ref. [27]). (B) Estimates of the quark–gluon plasma's (QGP's) electrical conductivity as a function of temperature [32,34,70–75,114–119] (the figure is from Ref. [75]). PHSD, parton–hadron–string dynamics; BAMPS, Boltzmann approach to multiparton scatterings model; CSPM, color string percolation model; SYM, supersymmetric Yang–Mills plasma.

The incomplete QGP electromagnetic response has also been studied using the Drude model with different relaxation times [29]. It was found that the relaxation time could be comparable to the lifetime of the external magnetic field, given typical values of conductivity and temperature in the QGP. As a result, the magnetic field at the early stage of the collision is suppressed by 2 orders of magnitude, as indicated by the solid lines in Fig. 7B. Additionally, the preequilibrium properties of the QGP play a decisive role in the magnetic field evolution, as studied within a kinetic framework by solving the coupled Boltzmann and Maxwell equations [10]. The results suggest a rapid drop in the magnetic field strength during the preequilibrium stage of the QGP, as shown in Fig. 7C. Furthermore, Yan and Huang [10] found that while a residual magnetic field persists in the equilibrated QGP at RHIC energies, it becomes negligible at LHC energies.

In addition, the QGP produced in noncentral heavy-ion collisions is the most vortical fluid observed in nature, with a vorticity of approximately 10^{21} s^{-1} at RHIC energies [76]. Recent studies suggest that this swirling QGP can induce an additional magnetic field aligned with the external field, effectively prolonging the lifetime of the magnetic field within the QGP [31]. This effect is more pronounced at lower collision energies, as illustrated in Fig. 8, which compares Au + Au collisions at $\sqrt{s_{NN}} = 7.7$ and 200 GeV.

Experimental Results of the Electromagnetic Field Effects

Experimental data can help constrain theoretical estimates of the QGP's complex electromagnetic response by analyzing the electromagnetic field's imprints on final-state particles detected in the experiment. Detectors in heavy-ion collision experiments are typically complex apparatuses composed of multiple subsystems, designed to capture collision events with maximum clarity. For example, the Solenoidal Tracker at RHIC (STAR) has a diameter of approximately 15 m to accommodate various subsystems for tracking, identifying, and measuring particles produced in collisions [77]. Figure 9 sketches the STAR detector, with engineers on the ground for scale. Detecting a magnetic field with a lifetime on the order of 10^{-24} s using a traditional magnetometer is extremely challenging. In heavy-ion collisions, the magnetic field's properties are inferred from the 4-momenta of final-state particles. By employing observables sensitive to different stages of the magnetic field, its evolution can be experimentally investigated. However, some of these observables, such as those related to the CME and heavy-flavor particles, require very large data samples due to their statistical demands. This section reviews measurements of the effects induced by electromagnetic fields in heavy-ion collisions.

Ultraperipheral collisions

In UPCs, the impact parameter exceeds twice the nuclear radius [78,79], as illustrated in Fig. 10A. Instead of engaging in strong interactions, the nuclei interact through their electromagnetic fields, which can be described as a high flux of energetic quasi-real photons [80–85]. Elastic scattering between photons in UPCs has been observed at the LHC [86], while di-electron production from inelastic photon–photon processes has been reported by RHIC experiments [48], shown in Fig. 10B. These results confirm the generation of an electromagnetic field by fast-moving ions. The transverse momentum distribution of produced di-electron pairs, $\mathbf{P}_\perp$, in UPCs, is sensitive to the spatial charge configuration of nuclei. Therefore, measuring di-electron $\mathbf{P}_\perp$ can help constrain the strength of the magnetic field generated by the charged protons within nuclei [49]. Figure 10C presents the magnetic field strength from fitting nuclear charge radius and skin depth extracted from experimental di-electron measurements [48]; the magnitudes are consistent with theoretical calculations using the Heavy Ion Jet INteraction Generator model [9].

Charge-dependent directed flow as a witness of the electromagnetic field

Many novel phenomena in heavy-ion collisions involve the magnetic field in the QGP, such as the CME and the chiral phase transition under a strong magnetic field. The charge-dependent

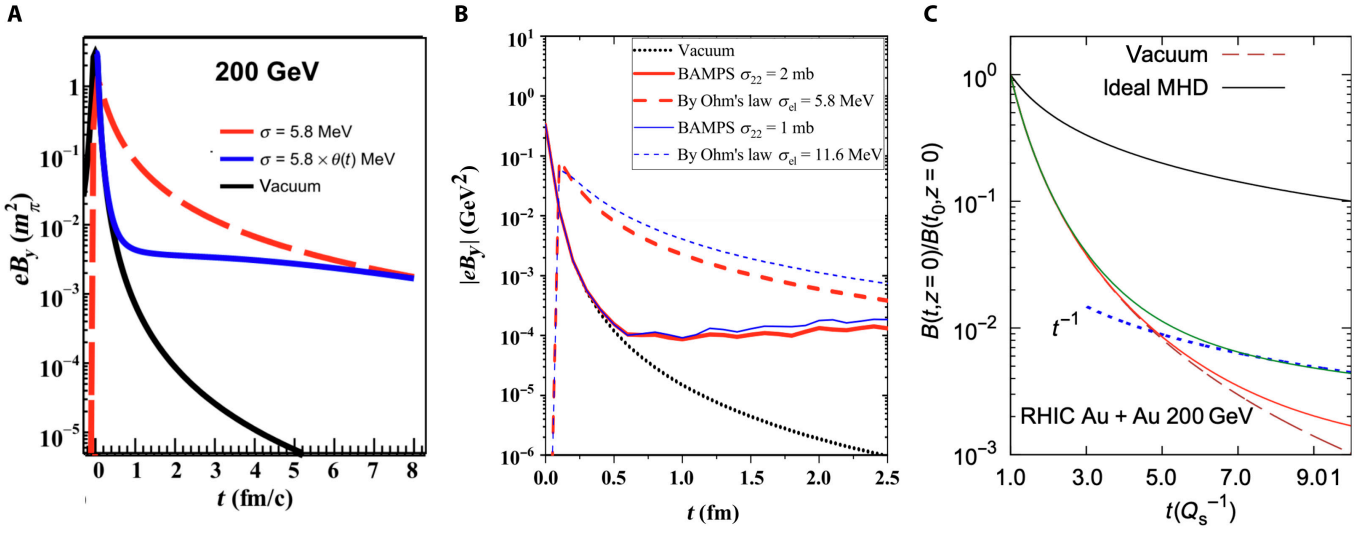

Fig. 7. The magnetic field evolution with (A) time-dependent conductivity (blue solid line; the figure is from Ref. [28]), (B) incomplete QGP electromagnetic response (blue and red solid lines; the figure is from Ref. [29]), and (C) in preequilibrium QGP (green solid line; the figure is from Ref. 10]) in Au + Au collisions at $\sqrt{s_{NN}}$ = 200 GeV. RHIC, Relativistic Heavy Ion Collider; MHD, magnetohydrodynamics.

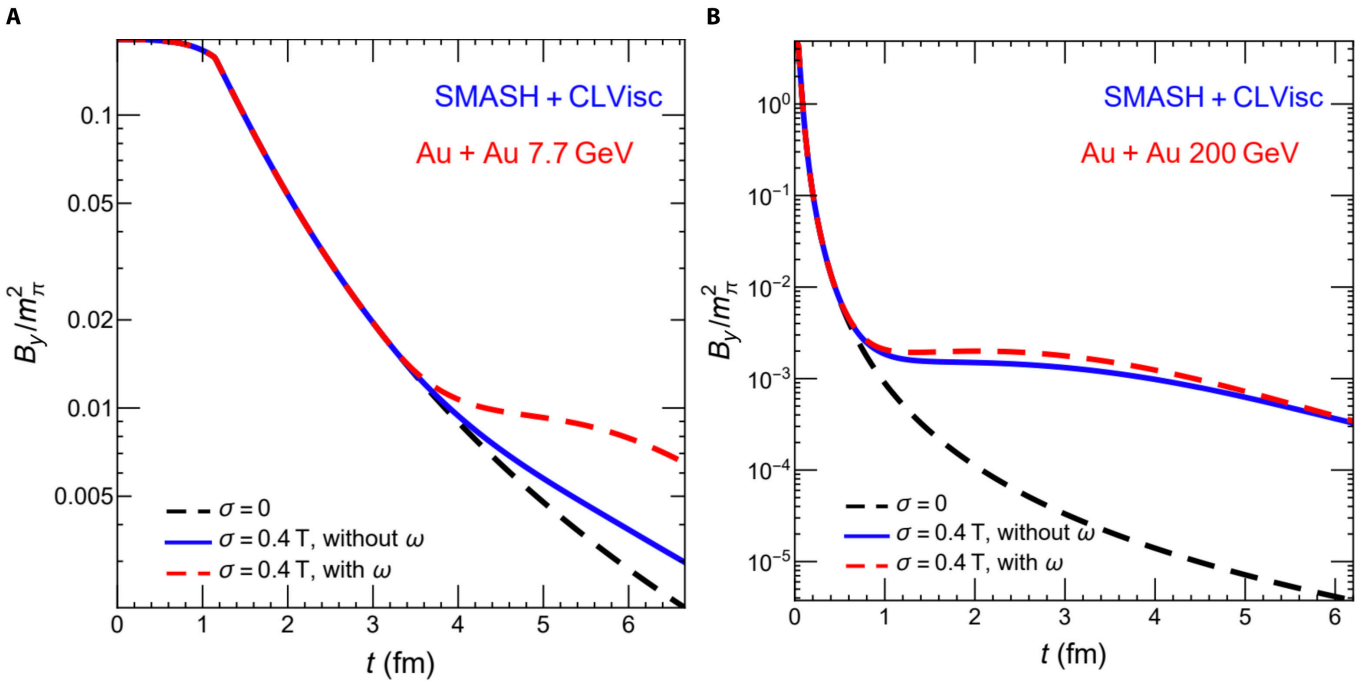

Fig. 8. The evolution of the magnetic field with and without vorticity contribution in Au + Au collisions at $\sqrt{s_{NN}}$ = (A) 7.7 and (B) 200 GeV, respectively (the figure is from Ref. [31]). SMASH, simulating many accelerated strongly interacting hadrons hadronic transport model; CLVisc, CCNU–LBNL (Central China Normal University–Lawrence Berkeley National Laboratory) viscous hydrodynamic model.

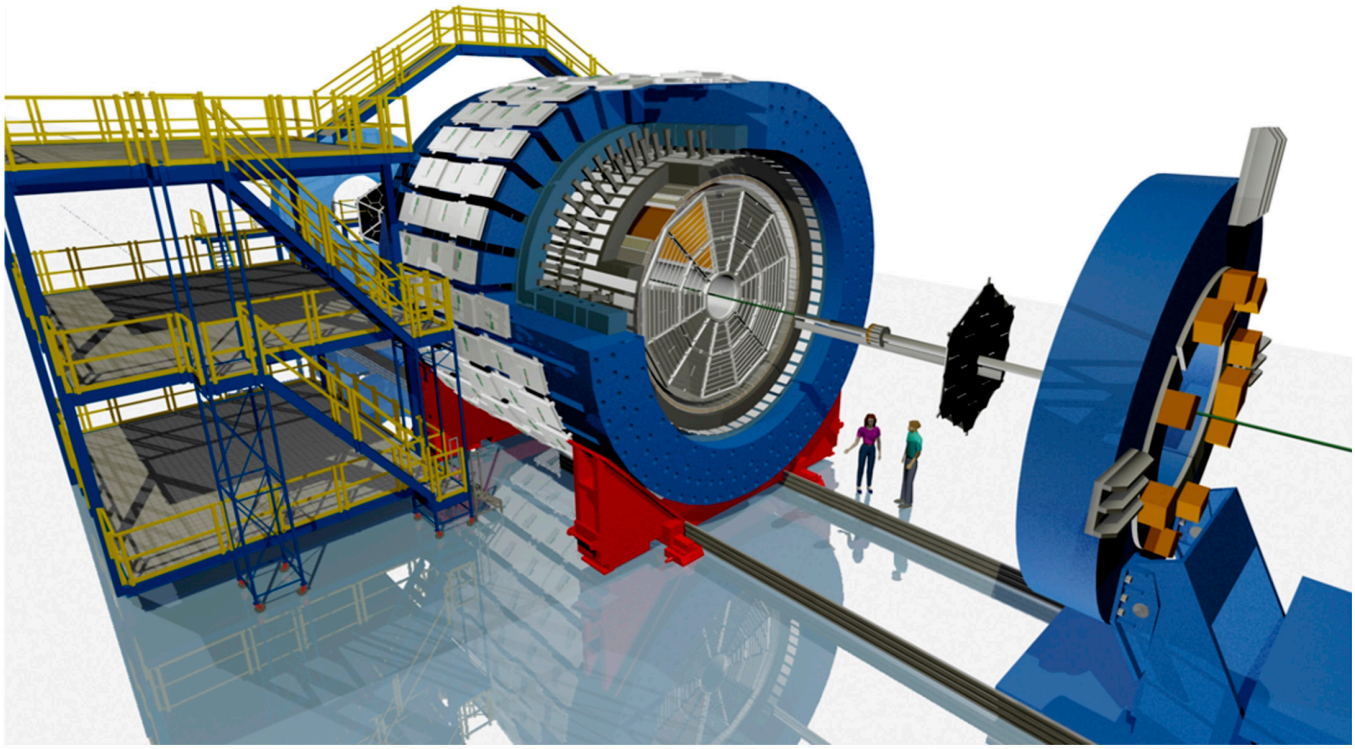

Fig. 9. Perspective view of the STAR detector (figure is from Alex Schmah in the Solenoidal Tracker at RHIC [STAR] collaboration).

collective motion of final-state particles can serve as a probe of the magnetic field in the medium, as charged particles in an electromagnetic field experience Lorentz and Coulomb forces, along with Faraday induction in the QGP, which collectively modify their momenta [39,41–46,87]. Figure 11 shows an overhead view of a heavy-ion collision. From this perspective, the system expansion influences the motion of oppositely charged particles similarly at leading order, while the electromagnetic fields introduce additional charge-dependent effects. The azimuthal angle (ϕ) distribution can be described by the following Fourier decomposition:

$$\frac{dN}{d\Delta\phi} \propto 1 + \sum_{n=1}^{\infty} 2v_n \cos n\Delta\phi, \tag{5}$$

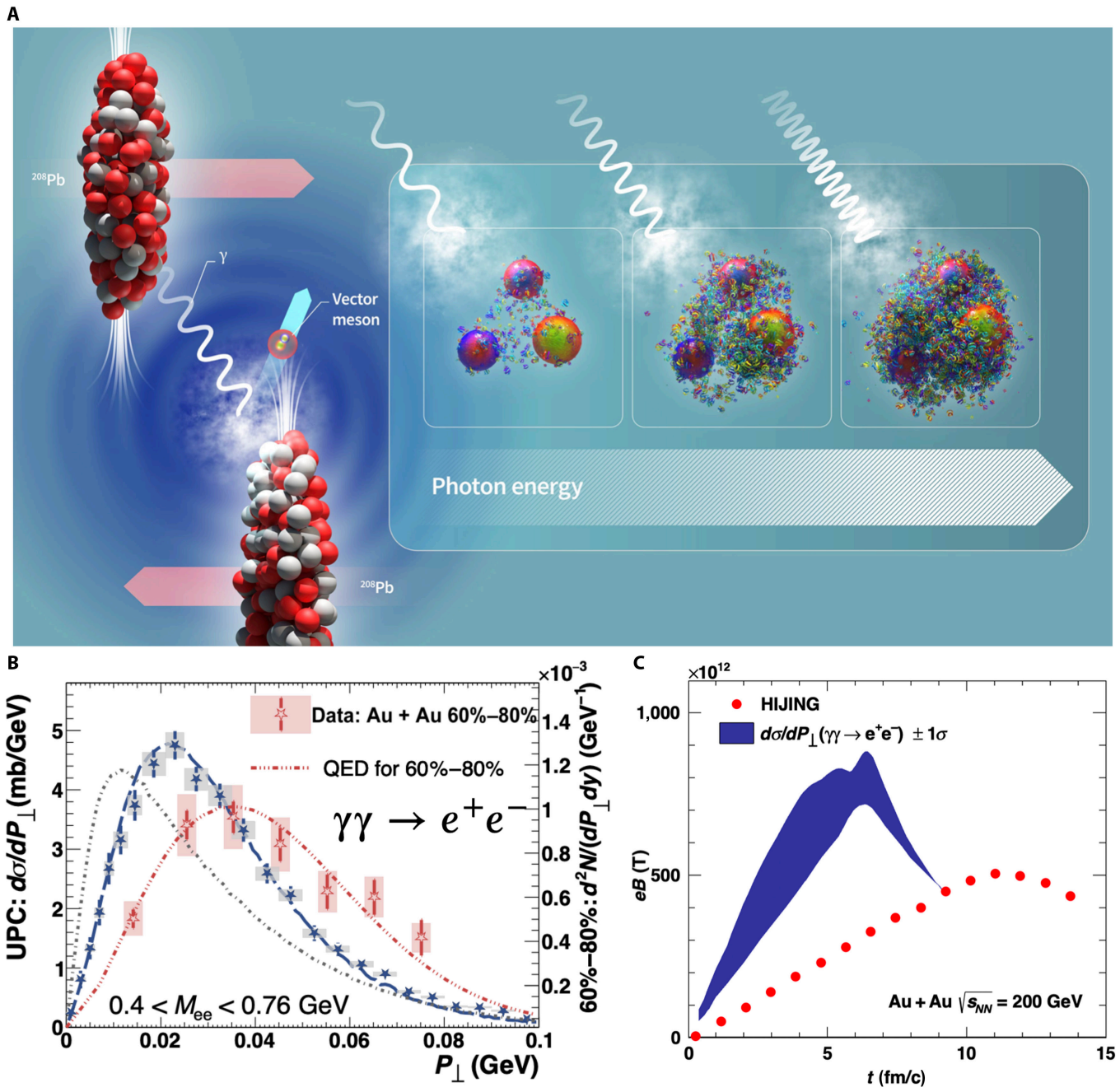

Fig. 10. (A) Sketch of an ultraperipheral collision (figure is from the European Organization for Nuclear Research [CERN]). (B) Di-electron $\mathbf{P}_\perp$ distribution in UPCs at the RHIC (the figure is from Ref. [48]). (C) The estimated magnetic field strength [49] (blue band) and the HIJING model calculations [9]. QED, quantum electrodynamics.

where $\Delta\phi$ is the azimuthal angle of a particle with respect to the reaction plane (spanned by the x and z axes as shown in Fig. 11) and v_n is the nth-harmonic flow coefficient. Directed flow v_1, arising from the initial tilt of the system, is an odd function of rapidity (y) and is sensitive to the rapidity-odd electromagnetic field generated by spectator protons [41,43–45,87].

The Hall effect from the Lorentz force, illustrated by the black lines in Fig. 11, increases v_1 for a positive charge moving forward ($y > 0$) and decreases it when moving backward ($y < 0$), enhancing the gradient dv_1/dy. For a negative charge, the effect is reversed, reducing dv_1/dy. Consequently, the difference $\Delta dv_1/dy$ between positive and negative charges is positive. Additionally, the rapid decay of the magnetic field in the medium induces an electric field via Faraday induction. Combined with the electric field from spectator protons, this results in a negative $\Delta dv_1/dy$ between positive and negative charges, as shown by the purplish red lines. Theoretical calculations [43–45] suggest that the combined effects of Faraday induction and Coulomb interactions are expected to dominate over the Hall effect for light quarks that are assumed to be in thermal equilibrium. On the other hand, for charm quarks, which form earlier and remain out of equilibrium, the effects are reversed [41]. Ultimately, these interactions will lead to a measurable difference in v_1 between positively and negatively charged hadrons via quark coalescence.

Recent v_1 measurements for protons and antiprotons exhibit a negative $\Delta dv_1/dy$, consistent with expectations from

Faraday induction and the Coulomb effect, in the 50% to 80% centrality range for Au + Au, Ru + Ru, and Zr + Zr collisions at $\sqrt{s_{NN}} = 200$ GeV, as well as for Au + Au collisions at $\sqrt{s_{NN}} = 27$ GeV, as shown in Fig. 12. For the first time in experiments, signals consistent with the electromagnetic field effect on the QGP have been observed in symmetric collisions, with significances exceeding 5σ. It is proposed that the $\Delta dv_1/dy$ of light quarks, such as u and d, is sensitive to the magnetic field at freeze-out [43,44]. The more negative $\Delta dv_1/dy$ at $\sqrt{s_{NN}} = 27$ GeV compared to that at $\sqrt{s_{NN}} = 200$ GeV suggests a stronger late-stage magnetic field at lower energies, likely due to the longer passage time of incident nuclei and the shorter lifetime of the QGP. Huang et al. [31] examined the magnetic field strength on the QGP freeze-out hypersurface at several collision energies available at the RHIC and found that the strength of the late-stage magnetic field is higher at lower energies regardless of the vorticity effect, as shown in Fig. 13. This result can explain the more negative $\Delta dv_1/dy$ measured at $\sqrt{s_{NN}} = 27$ GeV.

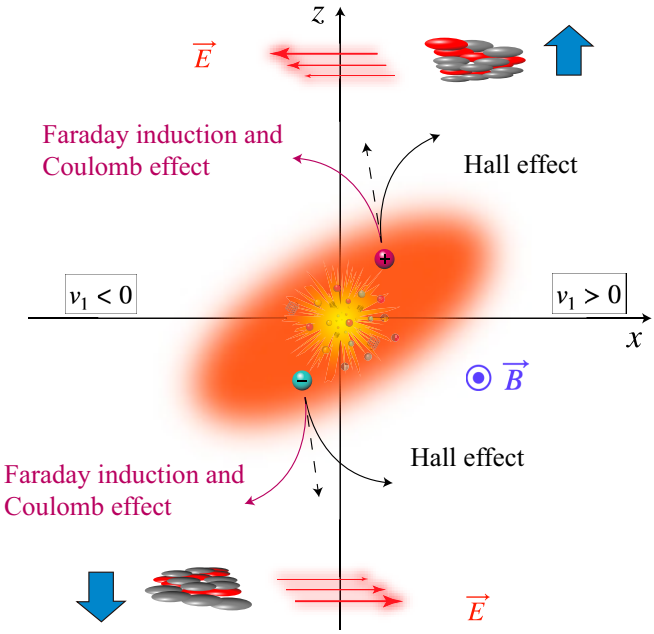

Fig. 11. Hall effect, Faraday induction, and Coulomb effect on the momenta of charged particles in a collision (the figure is from Ref. [113]).

Besides electromagnetic effects, quarks transported from the incident nucleons can also influence the $\Delta dv_1/dy$ between protons and antiprotons, as transported u and d quarks may contribute to proton formation through quark recombination. Different model studies [88–90] suggest that transported quarks give a positive contribution to proton $\Delta dv_1/dy$, hindering the observation of the electromagnetic effect on $\Delta dv_1/dy$ in central collisions, where the magnetic field is weak. Figure 14 shows the centrality dependence of $\Delta dv_1/dy$ for pions, kaons, and protons. The $\Delta dv_1/dy$ values for kaons and protons transition from positive in central collisions to negative in peripheral ones, reflecting the increasing dominance of magnetic field effects. A hydrodynamic model with an inhomogeneous baryon density

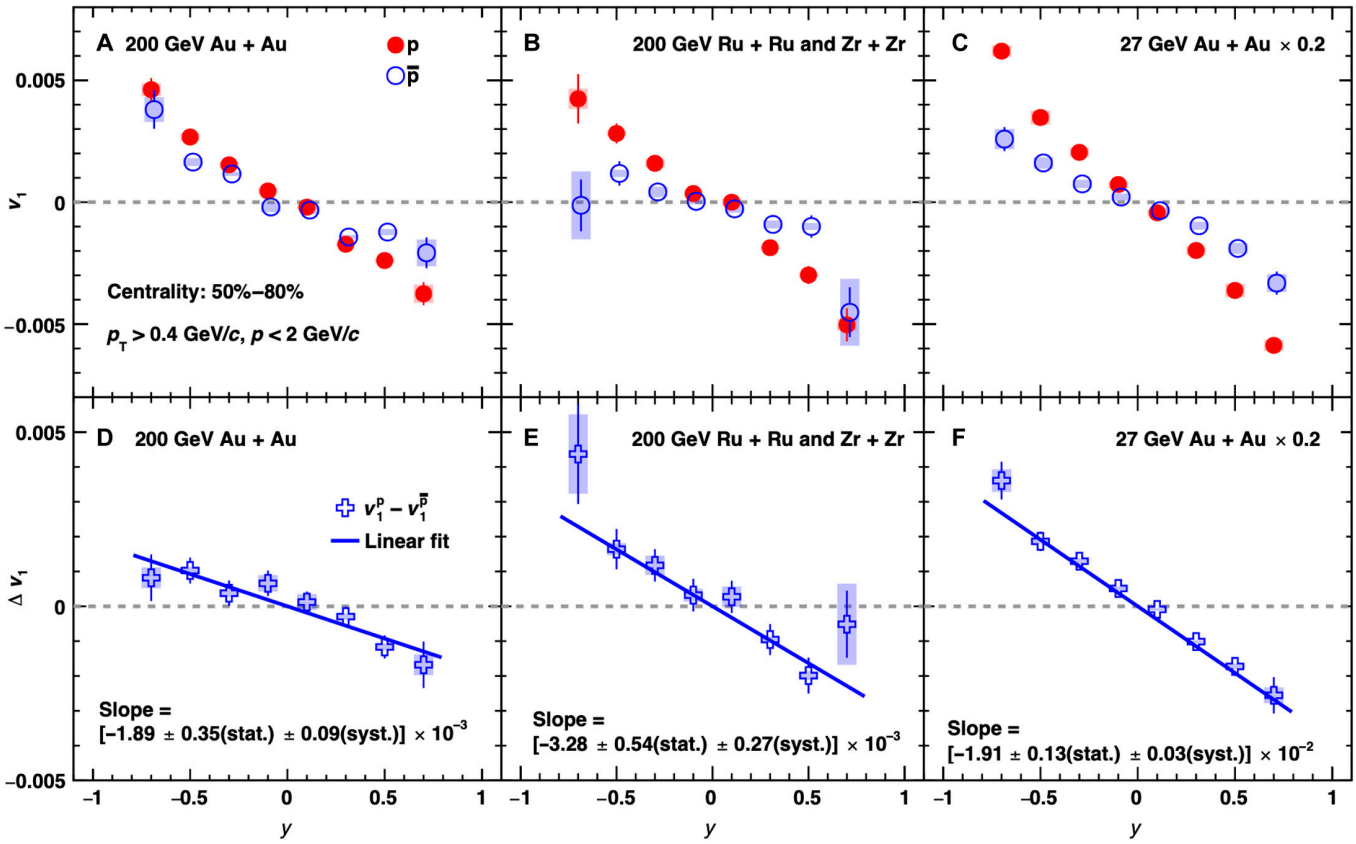

Fig. 12. Proton and antiproton directed flow in (A) Au + Au, (B) Ru + Ru and Zr + Zr collisions at $\sqrt{s_{NN}} = 200$ GeV and (C) Au + Au collisions at $\sqrt{s_{NN}} = 27$ GeV in the 50% to 80% centrality range (the figure is from Ref. [113]). Panels (D), (E), and (F) are the corresponding difference $\Delta dv_1/dy$ between protons and antiprotons.

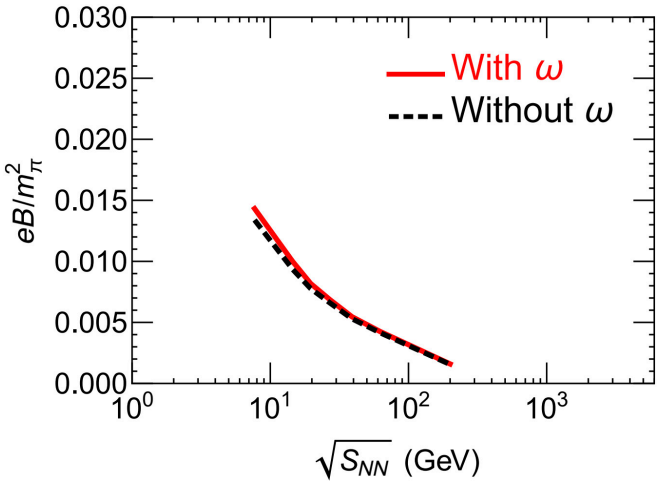

Fig. 13. The magnetic field strength on the freeze-out hypersurface at different collision energies (the figure is from Ref. [31]).

as the initial condition reproduces the proton $\Delta dv_1/dy$ but fails to simultaneously describe the pion and kaon data [91].

D^0 mesons are expected to be sensitive to the early-stage electromagnetic field, as charm quarks are heavy and produced early in the collisions [41]. Since the magnetic field is strongest in the early stage, theoretical calculations suggest that the directed flow splitting between D^0 and $\overline{D}^0$ is primarily driven by the Hall effect. Figure 15 shows the experimental results. Due to limited statistics, the measured $\Delta dv_1/dy$ between D^0 and $\overline{D}^0$ in Au + Au collisions at $\sqrt{s_{NN}} = 200$ GeV is consistent with both zero and the calculation with the electromagnetic field effect [92]. The results from Pb + Pb collisions at $\sqrt{s_{NN}} = 5.02$ TeV show a positive $\Delta dv_1/dy$, with a significance level below 3σ.

To avoid the contribution from transported quarks, the STAR Collaboration [93] examined combinations of hadrons that do not contain transported quarks and assumed the quark coalescence sum rule. Figure 16 shows that in the 10% to 40% centrality region, the measured $\Delta dv_1/dy$ between different hadron combinations with the same quark masses increases with both the charge difference and the difference in strangeness number. From the perspective of the electromagnetic field effect, the results suggest that the Hall effect is dominant in more central collisions or that it is the dominant effect for strange quarks at low energies.

In an asymmetric collision, where one of the nuclei has more protons, a net Coulomb field is directed from the larger nucleus to the smaller one [46,94,95]. This Coulomb field is an even function of rapidity and could generate a rapidity-even $\Delta dv_1/dy$ between positively and negatively charged quarks [46]. Since the net electric field originates from spectators, it exists only in the very early stages of the collisions. The charge-dependent directed flow in asymmetric collisions can reveal the electromagnetic properties of the system before equilibrium, such as the production time of charged quarks during the collisions. Figure 17 shows the $\Delta dv_1/dy$ between positively and negatively charged hadrons in Cu + Au collisions at $\sqrt{s_{NN}} = 200$ GeV [96]. The results are qualitatively consistent with the Coulomb effect, but the magnitudes are much smaller than the predictions from the parton–hadron–string dynamics model, suggesting that most of the quarks are produced at a later stage.

Global polarization of Λ ($\overline{\Lambda}$) under magnetic fields

Spin is an intrinsic property of particles, associated with the magnetic moment that interacts with external magnetic fields. Particles with opposite magnetic moments polarize in opposite directions, aligning with the external magnetic field. In heavy-ion collisions, besides the magnetic field, the substantial vorticity of the QGP can also induce global polarization through spin–orbital coupling in strong interactions [97–99]. On average, the direction of the magnetic field aligns with the global orbital angular momentum, resulting in quark polarization

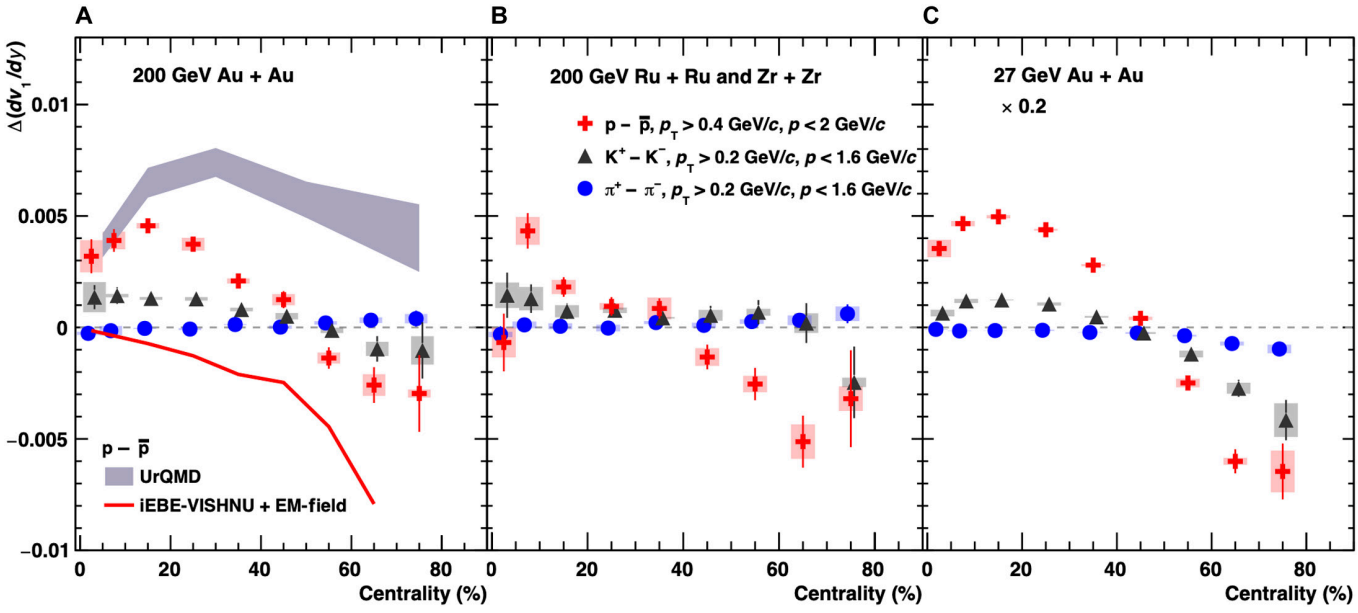

Fig. 14. $\Delta dv_1/dy$ between positively and negatively charged pions, kaons, and protons as a function of centrality in (A) Au + Au, (B) Ru + Ru and Zr + Zr collisions at $\sqrt{s_{NN}} = 200$ GeV, and (C) Au + Au collisions at $\sqrt{s_{NN}} = 27$ GeV (the figure is from Ref. [113]). UrQMD, ultrarelativistic quantum molecular dynamics; iEBE-VISHNU, event-by-event viscous Israel–Stewart hydrodynamics and UrQMD; EM-field, electromagnetic field.

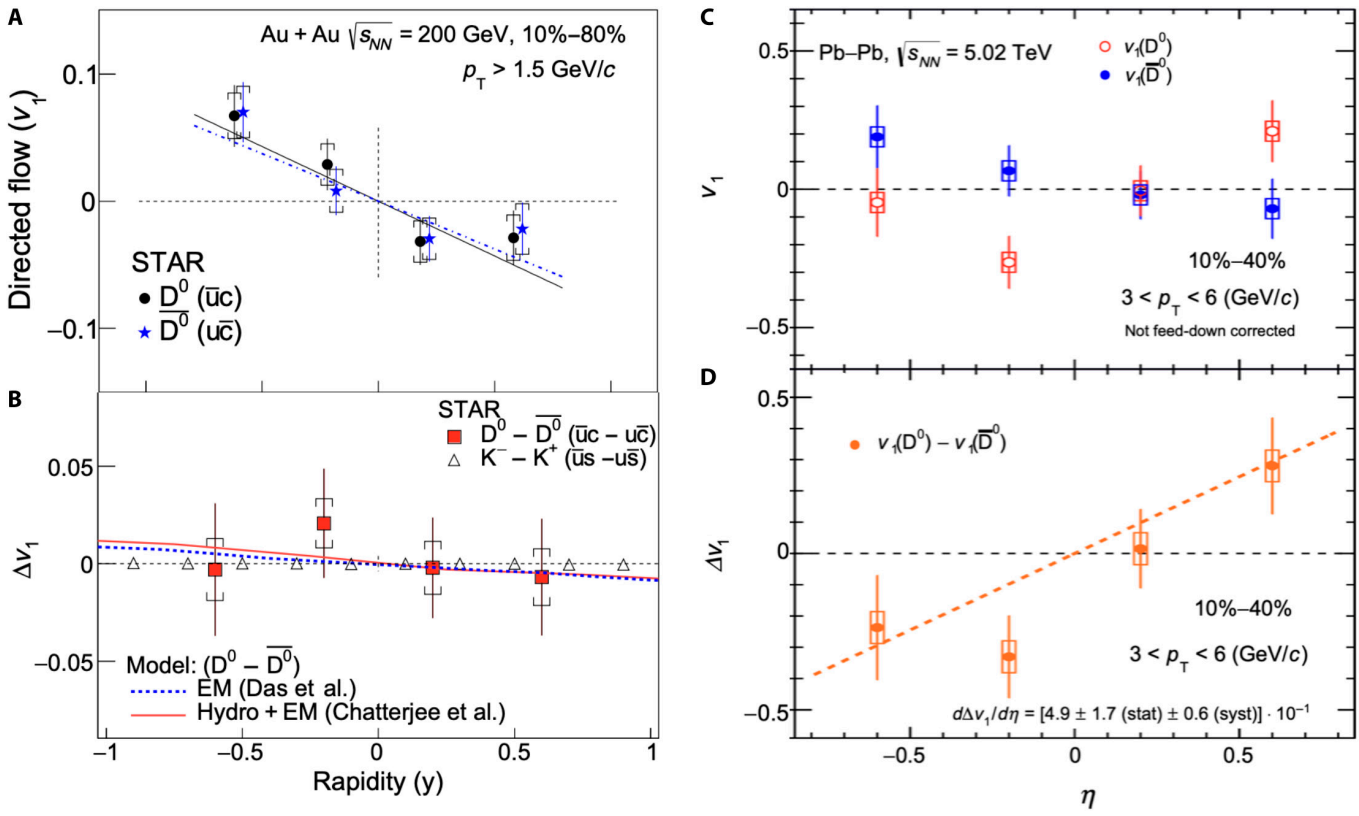

Fig. 15. (A) v_1 for D^0 and $\overline{D^0}$, as well as (B) the difference vs rapidity in Au + Au collisions at $\sqrt{s_{NN}}$ = 200 GeV [92]. (C) v_1 for D^0 and $\overline{D^0}$, as well as (D) the difference vs. pseudo-rapidity in Pb + Pb collisions at $\sqrt{s_{NN}}$ = 5.02 TeV (the figure is from Ref. [120]).

Index	quark mass	Δq	ΔS	Δv_1 combination	$F_\Delta \times 10^4$ (27 GeV)	$F_\Delta \times 10^4$ (200 GeV)
1	$\Delta m = 0$	0	0	$[\bar{p}(\bar{u}\bar{u}\bar{d}) + \phi(s\bar{s})] - [K^-(\bar{u}s) + \bar{\Lambda}(\bar{u}\bar{d}\bar{s})]$	$03 \pm 43 \pm 13$	$56 \pm 49 \pm 41$
2	$\Delta m \approx 0$	1	2	$[\bar{\Lambda}(\bar{u}\bar{d}\bar{s})] - [\frac{1}{3}\Omega^-(sss) + \frac{2}{3}\bar{p}(\bar{u}\bar{u}\bar{d})]$	$41 \pm 25 \pm 16$	$19 \pm 13 \pm 01$
3	$\Delta m \approx 0$	$\frac{4}{3}$	2	$[\bar{\Lambda}(\bar{u}\bar{d}\bar{s})] - [K^-(\bar{u}s) + \frac{1}{3}\bar{p}(\bar{u}\bar{u}\bar{d})]$	$39 \pm 07 \pm 03$	$16 \pm 05 \pm 03$
4	$\Delta m = 0$	2	6	$[\bar{\Omega}^+(\bar{s}\bar{s}\bar{s})] - [\Omega^-(sss)]$	$83 \pm 130 \pm 25$	$35 \pm 58 \pm 54$
5	$\Delta m \approx 0$	$\frac{7}{3}$	4	$[\bar{\Xi}^+(\bar{d}\bar{s}\bar{s})] - [K^-(\bar{u}s) + \frac{1}{3}\Omega^-(sss)]$	$64 \pm 36 \pm 19$	$26 \pm 20 \pm 04$

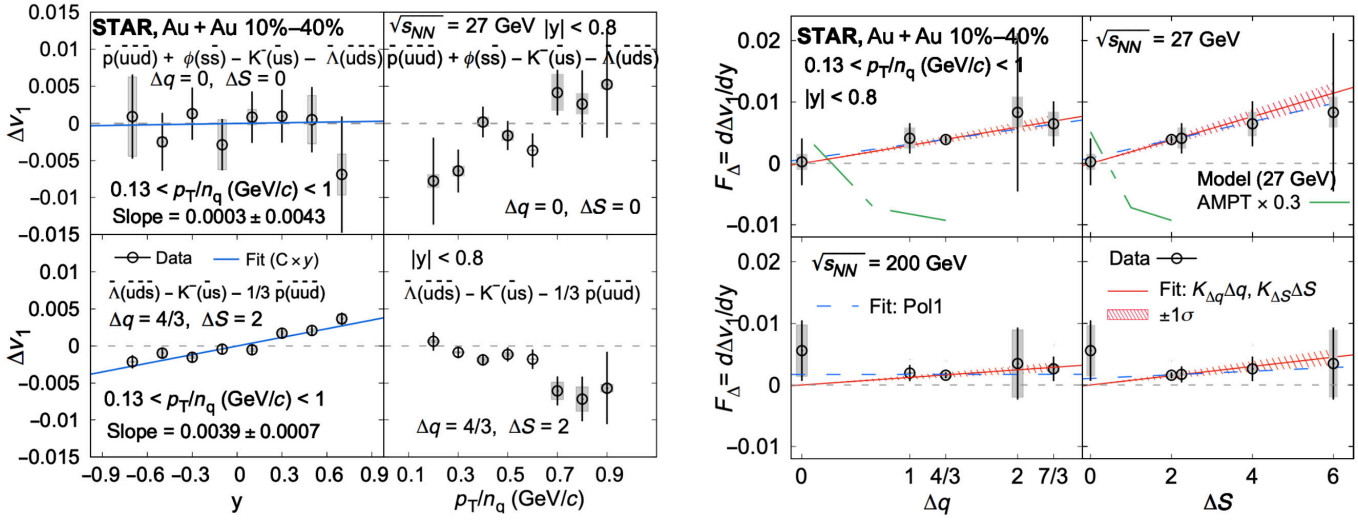

Fig. 16. $\Delta dv_1 / dy$ between different hadron combinations containing no transported quarks in 10% to 40% Au + Au collisions at $\sqrt{s_{NN}}$ = 27 GeV (the figure is from Ref. [93]).

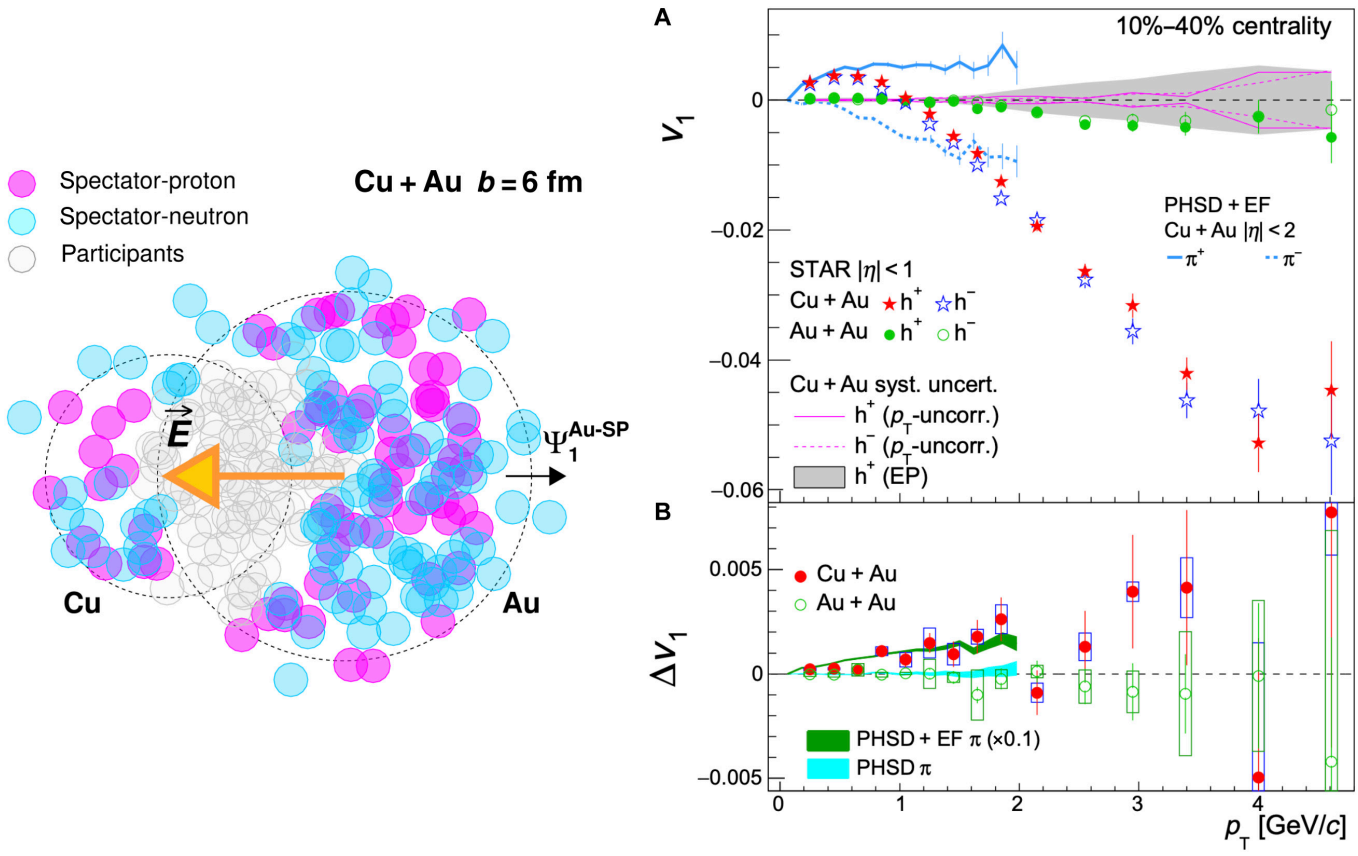

Fig. 17. v_1 for positive and negative charges (A) and the difference (B) in Cu + Au collisions at $\sqrt{s_{NN}}$ = 200 GeV (the figure is from Ref. [96]). EF, electric field; EP, event plane.

in approximately the same direction. However, while the magnetic field distinguishes particles and antiparticles, spin–orbital coupling does not exhibit such differentiation. The global polarization or spin alignment effect has been observed for Λ, $\bar{\Lambda}$, and ϕ in Au + Au collisions at the RHIC [76,100–106], as well as in Pb + Pb collisions at the LHC [107–109]. The measured polarizations for both hyperons and antihyperons are on the order of a few percent, with their difference,

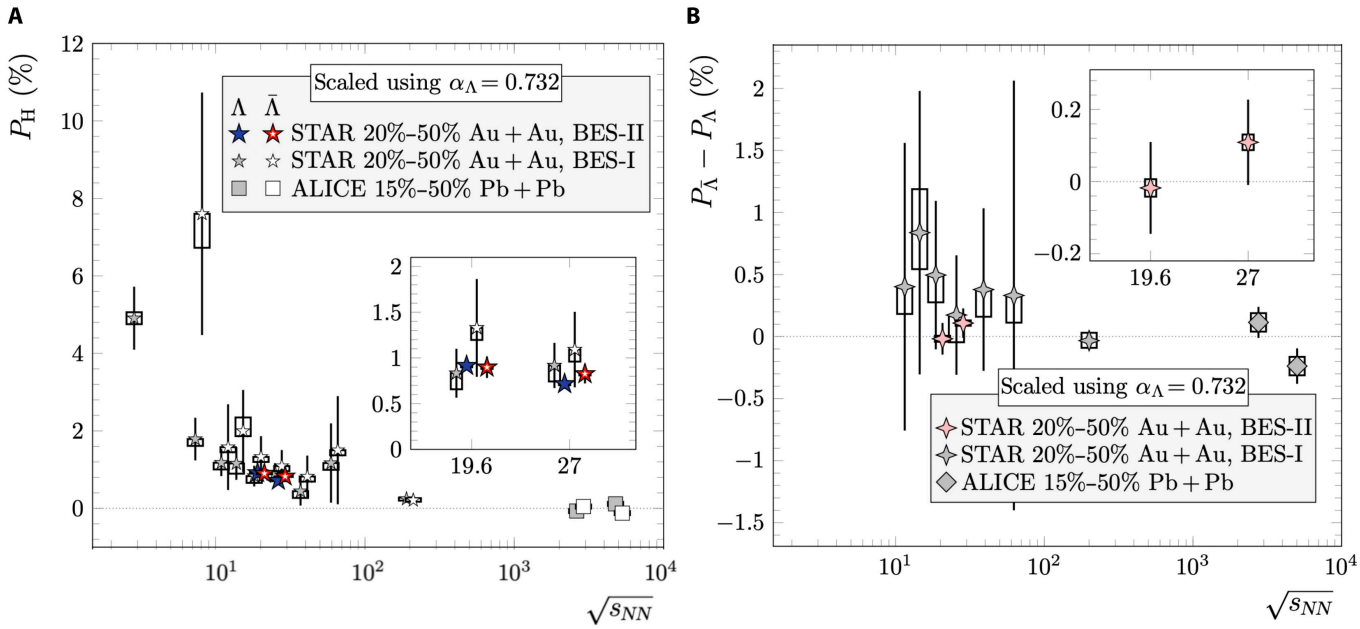

Fig. 18. Global polarizations of Λ and $\bar{\Lambda}$ (A) and the difference (B) in heavy-ion collisions [76,100,102,103,107] (the figure is from Ref. [102]). BES-I, Beam Energy Scan Phase I; BES-II, Beam Energy Scan Phase II.

$\Delta P_\Lambda = P_\Lambda - P_{\overline{\Lambda}}$, remaining within 1%, as shown in Fig. 18. The magnetic field strength can be estimated via [31,47,110,111]

$$\Delta P_\Lambda = 2\mu_\Lambda \frac{B}{T_\Lambda}, \tag{6}$$

where the magnetic moment of Λ is $\mu_\Lambda = 1.93 \times 10^{-14}$ MeV / T, and its freeze-out temperature is assumed to be $T_\Lambda = 150$ MeV. Based on the most accurate measurements from Au + Au collisions at $\sqrt{s_{NN}} = 19.6$ GeV, 27 GeV [100], and 200 GeV [102], the upper limits of the late-stage magnetic field at a 95% confidence level are 9.4×10^{16}, 1.4×10^{17}, and 6.0×10^{16} G for $\sqrt{s_{NN}} = 19.6$, 27, and 200 GeV, respectively. Comparing with Fig. 6, which illustrates the magnetic field evolution in Au + Au collisions at $\sqrt{s_{NN}} = 200$ GeV, we can infer that the electrical conductivity of the QGP, as predicted by lattice QCD calculations, is of the right magnitude. Moreover, the beam energy dependence of ΔP_Λ provides a means to probe the lifetime of the magnetic field across different collision energies. Early results from the RHIC Beam Energy Scan (BES) Phase I suggest an inverse relationship between the magnetic field lifetime and the beam energy [112]. With increased statistics from the RHIC BES Phase II program, the uncertainties in the energy dependence of ΔP_Λ can be further reduced.

Challenges and Opportunities

Maxwell's equations provide the most successful framework for describing electromagnetic fields. Based on these equations, a very strong magnetic field would arise in relativistic heavy-ion collisions. The peak value of this magnetic field is determined by the spatial distribution and velocity of the electric charges involved. For a given collision energy and impact parameter, the magnetic field strength in the vacuum can be reliably estimated theoretically. Although the initial charge distribution depends on the nuclear structure and carries some uncertainty, the peak magnetic field values in heavy-ion collisions are generally consistent across different assumptions about nuclear charge distributions [7,8,24,37]. However, the evolution of the magnetic field, particularly its interaction with the QGP, remains theoretically undetermined. In the early stages of the collision, different models predict markedly different magnetic field strengths, while their evolution curves tend to converge in the later stages, as illustrated in Fig. 7.

Experimental measurements of the magnetic field effects can provide insights into its evolution. For instance, the directed flow of D^0 mesons can probe the early-stage magnetic field [41]. However, early experimental results have large uncertainties, as shown in Fig. 15. The ALICE collaboration has collected several orders of magnitude more data in the Run 3 project compared with the previous D^0 meson v_1 publication, and results from this new dataset are highly anticipated. Meanwhile, the directed flow of light quarks is sensitive to the late-stage magnetic field [43–45]. The charge-splitting effect in light-hadron-directed flow has shown qualitative agreement with theoretical calculations. However, quantitative comparisons with theoretical models require full simulations incorporating both transported-quark effects and magnetic field effects, necessitating further theoretical work. Experimentally, measuring the charge-dependent directed flow of light hadrons at different collision energies can help explore the beam energy dependence of the magnetic field.

For the global polarization splitting between Λ and $\overline{\Lambda}$, current results are consistent with both the magnetic field evolution based on lattice QCD conductivity and the scenario with no magnetic field. In Run 2025, the STAR collaboration will collect 10 times more events from Au + Au collisions at $\sqrt{s_{NN}} = 200$ GeV. Results from this new dataset will provide stronger constraints on the late-stage magnetic field.

Moreover, new observables have recently been proposed to study the magnetic field in experiments, such as baryon electric charge correlation [53,54] and elliptic flow of direct photons [50]. Experimental measurements of these effects are eagerly anticipated.

Summary

This review article explores the intense electromagnetic fields generated in heavy-ion collisions at relativistic energies, where accelerated nuclei create high-temperature environments leading to quark deconfinement. These fields, with strengths reaching 10^{18} G at the RHIC and 10^{19} G at the LHC, can profoundly impact the produced particles and serve as a tool to investigate the electromagnetic properties of the QGP. We have presented a comprehensive overview of the magnetic field generated in heavy-ion collisions, covering its generation, evolution, and experimental status. While the peak value of the magnetic field is relatively well constrained theoretically, its evolution within the QGP remains an open question. Experimental measurements of magnetic field effects at various stages are essential for mapping out this evolution. For instance, the directed flow of D^0 mesons is believed to be sensitive to the early-stage magnetic field. Although early measurements at the LHC suffer from large uncertainties, more precise D^0 meson v_1 data from the Run 3 program are expected to provide deeper insights into the early magnetic field dynamics. The article consolidates existing knowledge and serves as a comprehensive resource to compile most aspects of the magnetic field in this context. Additionally, we suggest future directions for further research in this area of nuclear and high-energy physics.

Acknowledgments

Funding: This work is supported in part by the National Key Research and Development Program of China under Contract No. 2022YFA1604900; the National Natural Science Foundation of China (NSFC) under Contract Nos. 12147101, 12205050, 12025501, and 12225502; Guangdong Major Project of Basic and Applied Basic Research No. 2020B0301030008; the STCSM under Grant No. 23590780100; and the Natural Science Foundation of Shanghai under Grant No. 23JC1400200. Gang Wang is supported by the US Department of Energy under Grant No. DE-FG02-88ER40424 and by the NSFC under Contract No. 1835002. Aihong Tang is supported by the US Department of Energy under Grant Nos. DE-AC02-98CH10886 and DE-FG02-89ER40531.
Author contributions: All authors contributed to the original draft and revisions.
Competing interests: The authors declare that they have no competing interests.

References

1. Shuryak EV. Quantum chromodynamics and the theory of superdense matter. *Phys Rep*. 1980;61(2):71.
2. Kolb E. *The early universe*. 1st ed. Boca Raton (FL): CRC Press; 1990.
3. Ko CM. Searching for QCD critical point with light nuclei. *Nucl Sci Tech*. 2023;34(5):80.
4. Chen JH, Dong X, He XH, Huang HZ, Liu F, Luo XF, Ma YG, Ruan LJ, Shao M, Shi SS, et al. Properties of the QCD matter—Review of selected results from the relativistic heavy ion collider beam energy scan (RHIC BES) program. *Nucl Sci Tech*. 2024;35(12):Article 214.
5. Shou QY, Ma YG, Zhang S, Zhu JH, Mao YX, Pei H, Yin ZB, Zhang XM, Zhou DC, Peng XY, et al. Properties of QCD matter: A review of selected results from ALICE experiment. *Nucl Sci Tech*. 2024;35(12):219.
6. Liu Y-C, Huang X-G. Anomalous chiral transports and spin polarization in heavy-ion collisions. *Nucl Sci Tech*. 2020;31(6):56.
7. Skokov V, Illarionov AY, Toneev V. Estimate of the magnetic field strength in heavy-ion collisions. *Int J Mod Phys A*. 2009;24(31):5925–5932.
8. Kharzeev DE, McLerran LD, Warringa HJ. The effects of topological charge change in heavy ion collisions: "Event by event P and CP violation". *Nucl Phys A*. 2008;803:227–253.
9. Deng W-T, Huang X-G. Event-by-event generation of electromagnetic fields in heavy-ion collisions. *Phys Rev*. 2012;85(4):044907.
10. Yan L, Huang X-G. Dynamical evolution of a magnetic field in the preequilibrium quark-gluon plasma. *Phys Rev*. 2023;107(9):094028.
11. Fukushima K, Kharzeev DE, Warringa HJ. The chiral magnetic effect. *Phys Rev D*. 2008;78(7):074033.
12. Kharzeev DE, Liao J, Voloshin SA, Wang G. Chiral magnetic and vortical effects in high-energy nuclear collisions—A status report. *Prog Part Nucl Phys*. 2016;88:1–28.
13. Kharzeev DE, Liao J, Tribedy P. Chiral magnetic effect in heavy ion collisions: The present and future. *Int J Mod Phys E*. 2024;33(09):2430007.
14. Kharzeev DE, Liao J. Chiral magnetic effect reveals the topology of gauge fields in heavy-ion collisions. *Nature Rev Phys*. 2021;3(1):55–63.
15. Gusynin VP, Miransky VA, Shovkovy IA. Catalysis of dynamical flavor symmetry breaking by a magnetic field in (2+1)-dimensions. *Phys Rev Lett*. 1994;73(26):3499.
16. Bali GS, Bruckmann F, Endrodi G, Fodor Z, Katz SD, Krieg S, Schafer A, Szabo KK. The QCD phase diagram for external magnetic fields. *J High Energy Phys*. 2012;2012(2):044.
17. Bali GS, Bruckmann F, Endrodi G, Fodor Z, Katz SD, Schafer A. QCD quark condensate in external magnetic fields. *Phys Rev D*. 2012;86(7):071502.
18. Mizher AJ, Chernodub MN, Fraga ES. Phase diagram of hot QCD in an external magnetic field: Possible splitting of deconfinement and chiral transitions. *Phys Rev D*. 2010;82:105016.
19. Fraga ES, Mizher AJ. Chiral transition in a strong magnetic background. *Phys Rev D*. 2008;78:025016.
20. Endrodi G. Critical point in the QCD phase diagram for extremely strong background magnetic fields. *J High Energy Phys*. 2015;2015(07):173.
21. Bigdeli M. Neutrons in strong magnetic fields and equation of state of neutron matter. *Phys Rev C*. 2017;95:024309.
22. Yakhshiev U, Kim H-C, Oka M. Nucleon and Δ isobar in a strong magnetic field. *Phys Rev D*. 2019;99:054027.
23. Andreichikov MA, Kerbikov BO, Orlovsky VD, Simonov YA. Neutron in strong magnetic fields. *Phys Rev D*. 2014;89(7):074033.
24. Zhao X-L, Ma G-L, Ma Y-G. Impact of magnetic-field fluctuations on measurements of the chiral magnetic effect in collisions of isobaric nuclei. *Phys Rev C*. 2019;99(3):034903.
25. Zhao J, Chen JH, Huang XG, Ma YG. Electromagnetic fields in ultra-peripheral relativistic heavy-ion collisions. *Nucl Sci Tech*. 2024;35(2):20.
26. Tuchin K. Initial value problem for magnetic fields in heavy ion collisions. *Phys Rev C*. 2016;93(1):014905.
27. Huang A, She D, Shi S, Huang M, Liao J. Dynamical magnetic fields in heavy-ion collisions. *Phys Rev C*. 2023;107(3):034901.
28. Li H, Xia X-L, Huang X-G, Huang HZ. Dynamic calculations of magnetic field and implications on spin polarization and spin alignment in heavy ion collisions. *Phys Rev C*. 2023;108:044902.
29. Wang Z, Zhao J, Greiner C, Xu Z, Zhuang P. Incomplete electromagnetic response of hot QCD matter. *Phys Rev C*. 2022;105(4):L041901.
30. Zhang J-J, Sheng X-L, Pu S, Chen J-N, Peng G-L, Wang J-G, Wang Q. Charge-dependent directed flows in heavy-ion collisions by Boltzmann-Maxwell equations. *Phys Rev Res*. 2022;4(3):033138.
31. Huang A, Wu X-Y, Huang M. Effect of vorticity on the dynamical magnetic fields in heavy-ion collisions. *Phys Rev D*. 2024;110(9):094032.
32. Ding HT, Francis A, Kaczmarek O, Karsch F, Laermann E, Soeldner W. Thermal dilepton rate and electrical conductivity: An analysis of vector current correlation functions in quenched lattice QCD. *Phys Rev D*. 2011;83(3):034504.
33. Francis A, Kaczmarek O. On the temperature dependence of the electrical conductivity in hot quenched lattice QCD. *Prog Part Nucl Phys*. 2012;67(2):212–217.
34. Amato A, Aarts G, Allton C, Giudice P, Hands S, Skullerud J-I. Electrical conductivity of the quark-gluon plasma across the deconfinement transition. *Phys Rev Lett*. 2013;111(17):172001.
35. Guo X, Liao J, Wang E. Spin hydrodynamic generation in the charged subatomic swirl. *Sci Rep*. 2020;10(1):2196.
36. McLerran L, Skokov V. Comments about the electromagnetic field in heavy-ion collisions. *Nucl Phys A*. 2014;929:184–190.
37. Voronyuk V, Toneev VD, Cassing W, Bratkovskaya EL, Konchakovski VP, Voloshin SA. Electromagnetic field evolution in relativistic heavy-ion collisions. *Phys Rev C*. 2011;83(5):Article 054911.
38. Stewart E, Tuchin K. Continuous evolution of electromagnetic field in heavy-ion collisions. *Nucl Phys A*. 2021;1016:122308.
39. Mohapatra RK, Saumia PS, Srivastava AM. Enhancement of flow anisotropies due to magnetic field in relativistic heavy-ion collisions. *Mod Phys Lett A*. 2011;26(33):2477.
40. Tuchin K. On viscous flow and azimuthal anisotropy of quark–gluon plasma in strong magnetic field. *J Phys G*. 2012;39(2):025010.
41. Das SK, Plumari S, Chatterjee S, Alam J, Scardina F, Greco V. Directed flow of charm quarks as a witness of the initial

strong magnetic field in ultra-relativistic heavy ion collisions. *Phys Lett B*. 2017;768:260–264.
42. Dubla A, Gürsoy U, Snellings R. Charge-dependent flow as evidence of strong electromagnetic fields in heavy-ion collisions. *Mod Phys Lett A*. 2020;35(39):2050324.
43. Charge-dependent flow induced by magnetic and electric fields in heavy ion collisions. *Phys Rev C*. 2018;98(5):055201.
44. Gursoy U, Kharzeev D, Rajagopal K. Magnetohydrodynamics, charged currents and directed flow in heavy ion collisions. *Phys Rev C*. 2014;89(5):054905.
45. Nakamura K, Miyoshi T, Nonaka C, Takahashi HR. Charge-dependent anisotropic flow in high-energy heavy-ion collisions from a relativistic resistive magneto-hydrodynamic expansion. *Phys Rev C*. 2023;107(3):034912.
46. Voronyuk V, Toneev VD, Voloshin SA, Cassing W. Charge-dependent directed flow in asymmetric nuclear collisions. *Phys Rev C*. 2014;90(6):064903.
47. Peng H-H, Wu S, Wang R-J, She D, Pu S. Anomalous magnetohydrodynamics with temperature-dependent electric conductivity and application to the global polarization. *Phys Rev D*. 2023;107:096010.
48. Adam J, Adamczyk L, Adams JR, Adkins JK, Agakishiev G, Aggarwal MM, Ahammed Z, Alekseev I, Anderson DM, Aparin A, et al. Measurement of e^+e^- momentum and angular distributions from linearly polarized photon collisions. *Phys Rev Lett*. 2021;127(5):052302.
49. Brandenburg JD, Zha W, Xu Z. Mapping the electromagnetic fields of heavy-ion collisions with the Breit-Wheeler process. *Eur Phys J A*. 2021;57(10):299.
50. Sun J-A, Yan L. Estimating the magnetic field strength in heavy-ion collisions via direct photon elliptic flow. *Phys Rev C*. 2024;109(3):034917.
51. Acharya S, ALICE Collaborations. Direct photon elliptic flow in Pb–Pb collisions at $\sqrt{s_{\mathrm{NN}}} = 2.76$ TeV. *Phys Lett B*. 2019;789:308.
52. Adare A, Afanasiev S, Aidala C, Ajitanand NN, Akiba Y, Akimoto R, al-Bataineh H, Alexander J, Alfred M, al-Ta'ani H, et al. Azimuthally anisotropic emission of low-momentum direct photons in Au + Au collisions at $\sqrt{s_{NN}} =$ 200 GeV. *Phys Rev C*. 2016;94(6):Article 064901.
53. Ding H-T, Gu J-B, Kumar A, Li S-T, Liu J-H. Baryon electric charge correlation as a magnetometer of QCD. *Phys Rev Lett*. 2024;132(20):201903.
54. Huang XG. Quantifying the strength of magnetic fields using baryon electric charge correlation. *Nucl Sci Tech*. 2024;35:138.
55. Huang X-G. Electromagnetic fields and anomalous transports in heavy-ion collisions—A pedagogical review, Rept. *Prog Phys*. 2016;79(7):076302.
56. Shou QY, Ma Y, Sorensen P, Tang A, Videbæk F, Wang H. Parameterization of deformed nuclei for Glauber modeling in relativistic heavy ion collisions. *Phys Lett B*. 2015;749:215–220.
57. Abdulhamid MI, STAR Collaboration. Imaging shapes of atomic nuclei in high-energy nuclear collisions. *Nature*. 2024;635:67–72.
58. Giacalone G. Beyond axial symmetry: High-energy collisions unveil the ground-state shape of ^{238}U. *Nucl Sci Tech*. 2024;35(12):218.
59. Xu H-J, Zhao J, Wang F. Hexadecapole deformation of ^{238}U from relativistic heavy-ion collisions using a nonlinear response coefficient. *Phys Rev Lett*. 2024;132(26):Article 262301.
60. Wang Z, Chen J, Xu H-J, Zhao J. Systematic investigation of the nuclear multipole deformations in U + U collisions with a multi-phase transport model. *Phys Rev C*. 2024;110(10):034907.
61. Schenke B. Violent collisions can reveal hexadecapole deformation of nuclei. *Nucl Sci Tech*. 2024;35(7):115.
62. Kouveliotou C, Dieters S, Strohmayer T, van Paradijs J, Fishman GJ, Meegan CA, Hurley K, Kommers J, Smith I, Frail D, et al. An X-ray pulsar with a superstrong magnetic field in the soft gamma-ray repeater SGR 1806-20. *Nature*. 1998;393(6682):235–237.
63. Siddique I, Sheng X-L, Wang Q. Space-average electromagnetic fields and electromagnetic anomaly weighted by energy density in heavy-ion collisions. *Phys Rev C*. 2021;104(3):034907.
64. Ma Y-G, Zhang S. Influence of nuclear structure in relativistic heavy-ion collisions. In: Tanihata I, Toki H, Kajino T, editors. *Handbook of nuclear physics*. Singapore: Springer Nature Singapore; 2023. p. 1485–1514.
65. Jia J, Giacalone G, Bally B, Brandenburg JD, Heinz U, Huang S, Lee D, Lee Y-J, Loizides C, et al. Imaging the initial condition of heavy-ion collisions and nuclear structure across the nuclide chart. *Nucl Sci Tech*. 2014;35(12):Article 220.
66. Cheng Y-L, Zhang S, Ma Y-G, Chen J, Zhong C. Electromagnetic field from asymmetric to symmetric heavy ion collision at 200 GeV/*c*. *Phys Rev C*. 2019;99(5):054906.
67. Bzdak A, Skokov V. Event-by-event fluctuations of magnetic and electric fields in heavy ion collisions. *Phys Lett B*. 2012;710(1):171.
68. Bloczynski J, Huang X-G, Zhang X, Liao J. Azimuthally fluctuating magnetic field and its impacts on observables in heavy-ion collisions. *Phys Lett B*. 2013;718(4–5):1529–1535.
69. Bloczynski J, Huang X-G, Zhang X, Liao J. Charge-dependent azimuthal correlations from AuAu to UU collisions. *Nucl Phys A*. 2015;939:85–100.
70. Buividovich PV, Chernodub MN, Kharzeev DE, Kalaydzhyan T, Luschevskaya EV, Polikarpov MI. Magnetic-field-induced insulator-conductor transition in *SU*(2) quenched lattice gauge theory. *Phys Rev Lett*. 2010;105(13):132001.
71. Burnier Y, Laine M. Towards flavour diffusion coefficient and electrical conductivity without ultraviolet contamination. *Eur Phys J C*. 2012;72:1–8.
72. Cassing W, Linnyk O, Steinert T, Ozvenchuk V. Electrical conductivity of hot QCD matter. *Phys Rev Lett*. 2013;110(18):182301.
73. Greif M, Bouras I, Greiner C, Xu Z. Electric conductivity of the quark-gluon plasma investigated using a perturbative QCD based parton cascade. *Phys Rev*. 2014;90(4):094014.
74. Finazzo SI, Noronha J. Holographic calculation of the electric conductivity of the strongly coupled quark-gluon plasma near the deconfinement transition. *Phys Rev D*. 2014;89(10):106008.
75. Sahoo P, Tiwari SK, Sahoo R. Electrical conductivity of hot and dense QCD matter created in heavy-ion collisions: A color string percolation approach. *Phys Rev D*. 2018;98(5):054005.
76. Adamczyk L, STAR Collaborations. Global Λ hyperon polarization in nuclear collisions: Evidence for the most vortical fluid. *Nature*. 2017;548(7665):62–65.
77. Ackermann K, Adams N, Adler C, Ahammed Z, Ahmad S, Allgower C, Amonett J, Amsbaugh J, Anderson BD, Anderson M, et al. STAR detector overview. *Nucl Instrum Methods Phys Res, Sect A*. 2003;499(2–3):624–632.
78. Bertulani CA, Baur G. Electromagnetic processes in relativistic heavy ion collisions. *Phys Rep*. 1988;163(5–6):299.

79. Natale AA, Roldao CG, Carneiro JPV. Two photon final states in peripheral heavy ion collisions. *Phys Rev C*. 2002;65(1):014902.
80. Baur G, Hencken K, Trautmann D, Sadovsky S, Kharlov Y. Coherent $\gamma\gamma$ and γA interactions in very peripheral collisions at relativistic ion colliders. *Phys Rep*. 2002;364(5):359–450.
81. Bertulani CA, Klein SR, Nystrand J. Physics of ultra-peripheral nuclear collisions. *Ann Rev Nucl Part Sci*. 2005;55(1):271.
82. Abdallah M, STAR Collaboration. Tomography of ultrarelativistic nuclei with polarized photon-gluon collisions. *Sci Adv*. 2023;9(1):Article eabq3903.
83. Ma YG. New type of double-slit interference experiment at fermi scale. *Nucl Sci Tech*. 2023;34(1):16.
84. Shao DY, Yan B, Yuan S-R, Zhang C. Spin asymmetry and dipole moments in τ-pair production with ultraperipheral heavy ion collisions. *Sci China-Phys Mech Astron*. 2024;67(8):281062.
85. Ma YG. A new idea of dipole moments in the tau lepton in ultra-peripheral heavy ion collisions. *Sci China Phys Mech Astron*. 2024;67:281061.
86. Aaboud M, ATLAS Collaboration. Evidence for light-by-light scattering in heavy-ion collisions with the ATLAS detector at the LHC. *Nature Phys*. 2017;13(1–2):852.
87. Sun Y, Plumari S, Das SK. Exploring the effects of electromagnetic fields and tilted bulk distribution on directed flow of D mesons in small systems. *Phys Lett B*. 2023;843:138043.
88. Guo Y, Liu F, Tang A. Directed flow of transported and nontransported protons in Au + Au collisions from ultrarelativistic quantum molecular dynamics model. *Phys Rev C*. 2012;86(4):Article 044901.
89. Nayak K, Shi S, Xu N, Lin Z-W. Energy dependence study of directed flow in Au + Au collisions using an improved coalescence in a multiphase transport model. *Phys Rev C*. 2019;100(5):054903.
90. Bozek P. Splitting of proton-antiproton directed flow in relativistic heavy-ion collisions. *Phys Rev C*. 2022;106(6):Article L061901.
91. Parida T, Chatterjee S. Baryon inhomogeneities driven charge dependent directed flow in heavy ion collisions. 2023. arXiv. https://doi.org/10.48550/arXiv.2305.08806
92. Adam J, Adamczyk L, Adams JR, Adkins JK, Agakishiev G, Aggarwal MM, Ahammed Z, Alekseev I, Anderson DM, Aoyama R, et al. First observation of the directed flow of D^0 and $\overline{D^0}$ in Au + Au collisions at $\sqrt{s_{NN}} = 200$ GeV. *Phys Rev Lett*. 2019;123:162301.
93. STAR Collaboration. Electric charge and strangeness-dependent directed flow splitting of produced quarks in Au+Au collisions. 2023. arXiv. https://doi.org/10.48550/arXiv.2304.02831
94. Hirono Y, Hongo M, Hirano T. Estimation of electric conductivity of the quark gluon plasma via asymmetric heavy-ion collisions. *Phys Rev C*. 2014;90(2):021903.
95. Deng W-T, Huang X-G. Electric fields and chiral magnetic effect in Cu+Au collisions. *Phys Lett B*. 2015;742:296–302.
96. Adamczyk L, STAR Collaborations. Charge-dependent directed flow in Cu + Au collisions at $\sqrt{s_{NN}} = 200$ GeV. *Phys Rev Lett*. 2017;118:012301.
97. Liang Z-T, Wang X-N. Globally polarized quark-gluon plasma in non-central $A + A$ collisions. *Phys Rev Lett*. 2005;94(10):102301.
98. Sun K-J, Liu D-N, Zheng Y-P, Chen J-H, Ko CM, Ma Y-G. Deciphering hypertriton and antihypertriton spins from their global polarizations in heavy-ion collisions. *Phys Rev Lett*. 2025;134(2):022301.
99. Chen J, Dong X, Ma Y-G, Xu Z. Measurements of the lightest hypernucleus ($^3_\Lambda$H): Progress and perspective. *Sci Bull*. 2023;68:3252–3260.
100. Abdulhamid MI, STAR Collaborations. Global polarization of Λ and $\overline{\Lambda}$ hyperons in Au + Au collisions at $\sqrt{s_{NN}} = 19.6$ and 27 GeV. *Phys Rev C*. 2023;108(1):014910.
101. Abdallah MS, STAR Collaboration. Pattern of global spin alignment of φ and K^{*0} mesons in heavy-ion collisions. *Nature*. 2023;614(7947):244–248.
102. Adam J, STAR Collaboration. Global polarization of Λ hyperons in Au + Au collisions at $\sqrt{s_{NN}} = 200$ GeV. *Phys Rev C*. 2018;98(1):014910.
103. Abdallah MS, STAR Collaborations. Global Λ-hyperon polarization in Au + Au collisions at $\sqrt{s_{\mathrm{NN}}} = 3$ GeV. *Phys Rev C*. 2021;104:Article L061901.
104. Abelev BI, STAR Collaboration. Spin alignment measurements of the $K^{*0}(892)$ and $\phi(1020)$ vector mesons in heavy ion collisions at $\sqrt{s_{NN}} = 200$ GeV. *Phys Rev C*. 2008;77(6):061902.
105. Chen J-H, Liang Z-T, Ma Y-G, Sheng X-L, Wang Q. Vector meson's spin alignments in high energy reactions. *Sci China Phys Mech Astron*. 2025;68(1):211001.
106. Chen JH, Liang ZT, Ma YG, Wang Q. Global spin alignment of vector mesons and strong force fields in heavy-ion collisions. *Sci Bull*. 2023;868(9):874–877.
107. Acharya S, ALICE Collaboration. Global polarization of Λ and $\overline{\Lambda}$ hyperons in Pb-Pb collisions at $\sqrt{s_{NN}} = 2.76$ and 5.02 TeV. *Phys Rev C*. 2020;101:044611.
108. Acharya S, ALICE Collaborations. Evidence of spin-orbital angular momentum interactions in relativistic heavy-ion collisions. *Phys Rev Lett*. 2020;125(1):012301.
109. Acharya S, ALICE Collaboration. Measurement of the J/ψ polarization with respect to the event plane in Pb-Pb collisions at the LHC. *Phys Rev Lett*. 2023;131(4):042303.
110. Müller B, Schäfer A. Chiral magnetic effect and an experimental bound on the late time magnetic field strength. *Phys Rev D*. 2018;98(7):071902.
111. Xu K, Lin F, Huang A, Huang M. $\Lambda/\overline{\Lambda}$ polarization and splitting induced by rotation and magnetic field. *Phys Rev D*. 2022;106(7):L071502.
112. Guo Y, Shi S, Feng S, Liao J. Magnetic field induced polarization difference between hyperons and anti-hyperons. *Phys Lett B*. 2019;798:134929.
113. Abdulhamid MI, Aboona BE, Adam J, Adams JR, Agakishiev G, Aggarwal I, Aggarwal MM, Ahammed Z, Aitbaev A, Alekseev I, et al. Observation of the electromagnetic field effect via charge-dependent directed flow in heavy-ion collisions at the Relativistic Heavy Ion Collider. *Phys Rev X*. 2024;14(1):011028.
114. Greif M, Greiner C, Denicol GS. Electric conductivity of a hot hadron gas from a kinetic approach. *Phys Rev D*. 2016;93(9):096012.
115. Caron-Huot S, Kovtun P, Moore GD, Starinets A, Yaffe LG. Photon and dilepton production in supersymmetric Yang-Mills plasma. *J High Energy Phys*. 2006;2006(12):015.
116. Gupta S. The electrical conductivity and soft photon emissivity of the QCD plasma. *Phys Lett B*. 2004;597(1):57–62.
117. Aarts G, Allton C, Foley J, Hands S, Kim S. Spectral functions at small energies and the electrical conductivity in hot, quenched lattice QCD. *Phys Rev Lett*. 2007;99:022002.

118. Thakur L, Srivastava PK, Kadam GP, George M, Mishra H. Shear viscosity η to electrical conductivity σ_{el} ratio for an anisotropic QGP. *Phys Rev D*. 2017;95(9):096009.
119. Puglisi A, Plumari S, Greco V. Shear viscosity η to electric conductivity σ_{el} ratio for the quark–gluon plasma. *Phys Lett B*. 2015;751:326–330.
120. Acharya S, Adamová D, Adler A, Adolfsson J, Aggarwal MM, Aglieri Rinella G, Agnello M, Agrawal N, Ahammed Z, Ahmad S, et al. Probing the effects of strong electromagnetic fields with charge-dependent directed flow in Pb-Pb collisions at the LHC. *Phys Rev Lett*. 2020;125(2):022301.